Computers & Fluids xxx (2014) xxx–xxx

Contents lists available at ScienceDirect

Computers & Fluids

journal homepage: www.elsevier.com/locate/compfluid

Numerical simulation of roughness effect on the stability of a hypersonic boundary layer

Kahei Danny Fong *, Xiaowen Wang, Xiaolin Zhong

University of California, 48-121 Engineering IV, 420 Westwood Plaza, Los Angeles, CA 90095-1597, USA

ARTICLE INFO

Article history:
Received 30 March 2013
Received in revised form 18 December 2013
Accepted 9 January 2014
Available online xxxx

Keywords:
Hypersonic boundary layer
Roughness
Cut-cell method
Transition
Receptivity

ABSTRACT

A new high-order cut-cell method is used to numerically simulate two dimensional roughness effects on modal growth in a hypersonic boundary layer. The steady base flow is simulated first by solving the compressible Navier–Stokes equations. Perturbations correspond to Mode S wave at 100 kHz and a wall normal velocity pulse with a continuous frequency spectrum up to 1 MHz are imposed onto the mean flow with roughness separately. A Fast Fourier Transform (FFT) is used to decompose the perturbation and to study the evolution of perturbations at different frequencies. The number of roughness elements in the boundary layer is changed for two test cases. Moreover, the effect of roughness height is studied in the Mode S simulation. It is found that when the roughness element is located at the synchronization point of a particular frequency (i.e. synchronization frequency), perturbations at frequencies higher than the synchronization frequency are damped. On the other hand, perturbations at frequencies lower than the synchronization frequency are amplified by the roughness. The same conclusion is drawn in cases where the roughness location is changed. The relation between roughness and the synchronization point is a candidate to explain roughness delayed transition seen experimentally.

1. Introduction

Transition can have a first-order impact on the lift and drag, stability and control, and heat transfer properties of air vehicles [1,2]. In particular, roughness induced transition is an important consideration in the design of thermal protection systems (TPS) of hypersonic vehicles [3]. A reentry vehicle entering the atmosphere initially experiences a heating environment associated with a laminar boundary layer. As the vehicle altitude decreases, the Reynold number increases and the boundary layer eventually becomes turbulent. The transition from a laminar boundary layer to a turbulent one can lead to an increase in surface heating rates by a factor of five or more. Thus, the ability to understand the physics of roughness induced transition plays an essential role in the design of TPS for reentry vehicles. Currently, roughness induced laminar–turbulent transition in hypersonic boundary layers, especially that induced by arbitrary surface roughness, is still poorly understood due to the limitation in experimental facilities and numerical methods [4].

Ideally, the laminar–turbulent transition process can be divided into four stages. The first stage involves small disturbance fields which are initialized by the viscous flow via a process termed receptivity. The initial disturbance fields can involve both free stream and vehicle self-induced fluctuations such as acoustics, dynamic vortices, and entropy spottiness. The next stage is the linear growth stage, where small disturbances are amplified until they reach a critical amplitude where nonlinear effects become important. The amplification can be in the form of exponential growth of eigen-modes (Tollmien–Schlichting waves or Mack waves) and non-modal growth of optimal disturbances (Transient growth). Once a disturbance has reached a finite amplitude, it often saturates and transforms the flow into a new and possibly unsteady state. This is termed the secondary instability stage. The last stage is the breakdown stage where nonlinearities and/or high-order instabilities excite an increasing number of scales and frequencies in the flow.

A receptivity study is mainly concerned with the excitation of instability waves where the characteristics can be analyzed by linear stability theory (LST) [5]. LST analyzes the propagation of individual sinusoidal waves in the streamwise direction inside the boundary layer. These waves are referred to Tollmien–Schlichting (T–S) waves for low speed flow. Their amplitudes vary through the boundary layer and die off exponentially outside the boundary layer. Extensive numerical and theoretical researches has been conducted to solve the linearized Navier–Stokes equations and many characteristics regarding the instability waves in hypersonic boundary layers have been discovered [5–9]. Mack [5] identified unstable modes using LST for compressible flow. He showed that inside a supersonic boundary layer, there are multiple higher

* Corresponding author. Tel.: +1 (310) 825 2905.
E-mail address: dannyfong@ucla.edu (K.D. Fong).

http://dx.doi.org/10.1016/j.compfluid.2014.01.009
0045-7930/

instability modes in addition to the first mode, which is the compressible counterpart of T–S waves in incompressible boundary layers. These instability modes in the supersonic boundary layer are termed the first mode, second mode, third mode, etc. For a supersonic boundary layer with a Mach number larger than four, Mack's second mode is the most unstable mode. It plays an important role in hypersonic boundary layer transition.

Direct numerical simulation has become an effective research tool for studying hypersonic boundary layer receptivity, stability, and transition by numerically solving the time-dependent three-dimensional Navier Stokes equations for temporally or spatially evolving instability waves. Malik et al. [10] investigated the responses of a Mach 8 flow over a sharp wedge of a half-angle of 5.3° to three types of external forcing: a planar free stream acoustic wave, a narrow acoustic beam enforced on the bow shock near the leading edge, and a blowing-suction slot on the wedge surface. They concluded that these three types of forcing eventually resulted in the same type of instability waves in the boundary layer. Ma and Zhong [11] studied the receptivity mechanisms of the same hypersonic boundary layer to various free stream disturbances, i.e., fast and slow acoustic waves, vorticity waves, and entropy waves, by solving the two-dimensional compressible Navier–Stokes equations. They found that the stable modes (i.e. Mode F) in the boundary layer played a very important role in the receptivity process. Recently, Wang et al. [12] further studied the response of a Mach 8 flow over a 5.3° half-angle sharp wedge to wall blowing and suction. The results showed that Mode S is strongly excited when the actuator is located upstream of the corresponding synchronization point. There is no significant amplification of pressure perturbation when the actuator is downstream of the synchronization point. Although the exact cause or mechanism of this result was not clear, such a result was obtained for wall blowing suction at all frequencies considered in their study. Balakumar [13] numerically investigated the receptivity of a two-dimensional roughness to acoustic waves and found that the isolated roughness does not contribute much in generating unstable disturbances. Marxen and Iaccarino [14] simulated the effects of a localized two-dimensional roughness element on disturbance amplification in a hypersonic boundary layer. Their numerical experiments showed that in the vicinity of the separation regions, which are located upstream and downstream of the roughness, an increased amplification of a second-mode disturbance occurs for a certain frequency.

Roughness has long been used to trip boundary layers to turbulence, but there have also been reports of experiments where roughness was found capable of stabilizing boundary layer. In 1964, Holloway and Sterrett [15] performed experiments on a boundary layer at Mach 4.0 and 6.0 with surface roughness at different local Reynolds numbers. They found that under certain circumstances, roughness with a height less than the boundary layer thickness can delay transition onset on a flat plate compared with the no roughness situation. Recently, Fujii investigated the effect of two dimensional surface roughness on a hypersonic boundary layer [16]. The experiment was carried out at the JAXA 0.5 m hypersonic wind tunnel using a 5° half angle sharp cone. It was found that wavy wall roughness can delay transition. To date, the exact cause of the delay is still unknown.

Previous DNS studies have shown that the roughness location plays an important role in the development of Mode S wave excited by a blowing suction slot [17]. It was found that the location of the synchronization point and the location of roughness are important factors in deciding roughness effect on transition [18]. Duan et al. [17] shows that when roughness is placed downstream of the synchronization point of one wave mode, that mode will be damped by roughness. However, if roughness is placed upstream of the synchronization point, the mode will be amplified. This could lead to an explanation of roughness delay transition as seen in experiments [15,16]. Thus, providing a way to control transition using two dimensional roughness may be possible. However, Duan et al. [17] only considered the roughness effect on one single frequency excited by blowing and suction. Moreover, only one roughness height was studied. In this paper, we further investigate the finite two dimensional roughness effect on perturbation growth over a Mach 5.92 flat plate boundary layer. To expand the studies of Duan et al. [17] and Fong et al. [19], the unsteady simulation model in this paper are a prue Mode S perturbation at 100 kHz and a wall normal velocity pulse. The wall normal velocity pulse has a frequency range of 1 MHz. The effect of roughness location and perturbation frequency is studied by decomposing the perturbations using FFT analysis. Moreover, the role of roughness heights and locations are also studied in the Mode S case.

2. Governing equations

For direct numerical simulation of hypersonic boundary layer transition, the governing equations are the three-dimensional Navier–Stokes equations. It is assumed that the flow is Newtonian fluid with the perfect gas assumption and isothermal wall conditions. The governing equations can be written in the following conservation-law form in Cartesian coordinates,

$$\frac{\partial U}{\partial t}+\frac{\partial F_j}{\partial x_j}+\frac{\partial F_{vj}}{\partial x_j}=0 \tag{1}$$

where U, F_j and F_{vj} are the vectors of flow variables, convective flux, and viscous flux in the spatial direction respectively. They are defined as

$$U=\{\rho,\rho u_1,\rho u_2,\rho u_3,e\} \tag{2}$$

$$F_j=\begin{Bmatrix}\rho u_j\\ \rho u_1u_j+p\delta_{1j}\\ \rho u_2u_j+p\delta_{1j}\\ \rho u_3u_j+p\delta_{1j}\\ (e+p)u_j\end{Bmatrix} \tag{3}$$

$$F_{vj}=\begin{Bmatrix}0\\ \tau_{1j}\\ \tau_{2j}\\ \tau_{3j}\\ \tau_{jk}u_k-q_j\end{Bmatrix} \tag{4}$$

In this paper, only perfect-gas hypersonic flow is considered, i.e.,

$$p=\rho RT \tag{5}$$

$$e=\rho\left(C_vT+\frac{1}{2}u_ku_k\right) \tag{6}$$

$$\tau_{ij}=\mu\left(\frac{\partial u_i}{\partial x_j}+\frac{\partial u_j}{\partial x_i}\right)+\delta_{ij}\lambda\frac{\partial u_k}{\partial x_k} \tag{7}$$

$$q_j=-k\frac{\partial T}{\partial x_j} \tag{8}$$

where R is the gas constant. The specific heat C_v is assumed to be constant with a given ratio of specific heats γ. The viscosity coefficient μ can be calculated by Sutherlands law in the form

$$\mu=\mu_r\left(\frac{T}{T_0}\right)^{3/2}\frac{T_0+T_s}{T+T_s} \tag{9}$$

where for air, $\mu_r=1.7894\times10^{-5}$ Ns/m^2, $T_0=288.0$ K, $T_s=110.33$ K and λ is assumed to be $-2/3\mu$. The heat conductivity

coefficient k can be computed through a constant Prandtl number.

3. High order cut-cell method

A schematic of a computational domain and a cut-cell grid with roughness is shown in Fig. 1. This figure shows a typical hypersonic flow over a blunt body, where a bow shock is created by the supersonic freestream. In this paper, a high-order shock-fitting method is used to track the movement of the bow shock which is treated as the upper boundary of the computational domain. The computational grid for a shock-fitting formulation is bounded by the bow shock above and the blunt body below. The cut-cell grid is a smooth curvilinear grid fitted to the baseline body shape without any roughness element. As a result, the roughness surface cuts across the grid lines. The roughness surface, Γ, is represented by the surface equation in the following form,

$$\Gamma: \ f(x,y,z) = 0 \tag{10}$$

For a problem concerning practical arbitrary roughness, it is likely that there is no analytical equation applicable to represent the shape of the roughness element. In this case, a set of n discrete points $\{(x_1,y_1,z_1),\ldots,(x_n,y_n,z_n)\}$ are used to represent the surface.

Both Eqs. (1) and (10) in the physical domain are transformed into a Cartesian computational domain bounded by the bow shock and flat plate. In the computational coordinate system, the body fitted grids are represented by curvilinear three-dimensional coordinates (ξ,η,ς) along the grid lines. The unsteady movement of the bow shock is treated as the computational upper boundary located at $\eta = \eta_{\max}$, which is time dependent. The other grid lines, $\varsigma = const$ and $\xi = const$, remain stationary during computations. The coordinate transformation is defined by:

$$\begin{cases} \xi = \xi(x,y,z) \\ \eta = \eta(x,y,z,t) \\ \varsigma = \varsigma(x,y,z) \\ \tau = t \end{cases} \leftrightarrow \begin{cases} x = x(\xi,\eta,\varsigma,\tau) \\ y = y(\xi,\eta,\varsigma,\tau) \\ z = z(\xi,\eta,\varsigma,\tau) \\ t = \tau \end{cases} \tag{11}$$

where (x,y,z,t) are the physical coordinates in the Cartesian coordinate system.

A third-order accurate cut cell method is used in the current numerical simulation [20]. A set of uniformly distributed Cartesian grids can be generated in the computational domain where the grid distribution in the physical domain is not uniformly distributed. Because smooth body-fitted grids are generated in the regular computational domain without roughness, some of the Cartesian grid cells may be cut by the roughness boundary, which leads to irregular Cartesian grid cells. More details of the grid structure and numerical detail are discussed previously in Duan et al. [20].

4. Results and discussion

4.1. Flow conditions and roughness model

The high order cut-cell method has been applied to model an isolated roughness on the surface of a hypersonic flat plate. Both

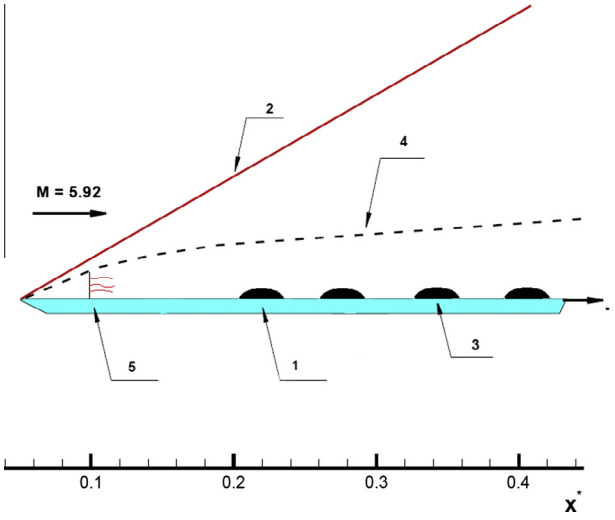

Fig. 2. A schematic of the problem: 1. Roughness; 2. Bow Shock; 3. Synchronization point; 4. Boundary layer; 5. Pure Mode S perturbation based on LST results, or wall normal velocity pulse.

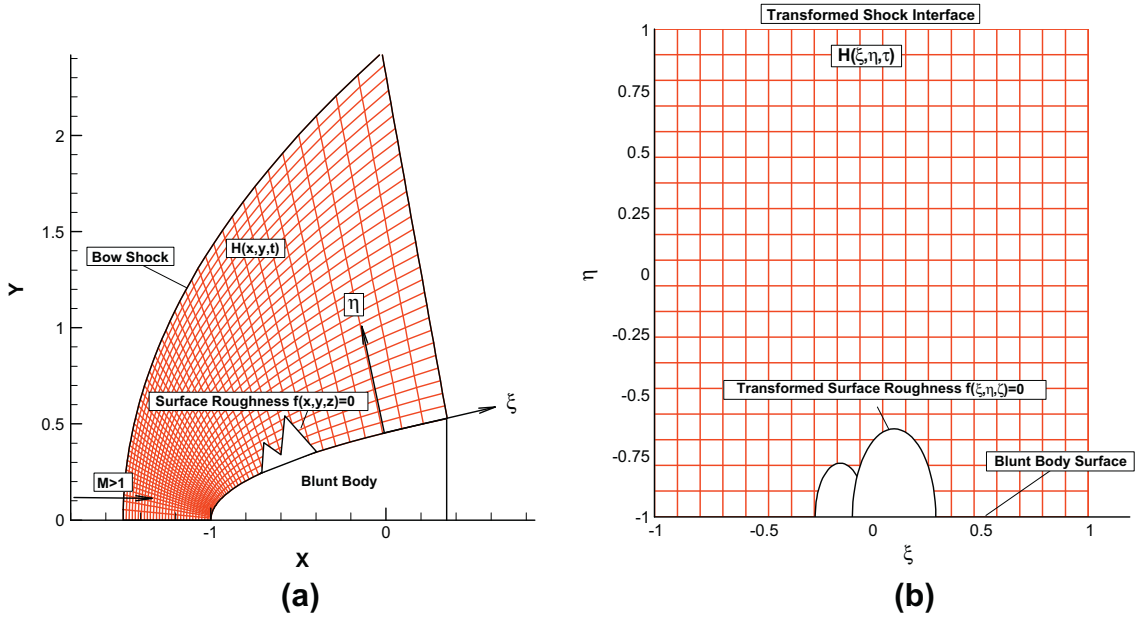

Fig. 1. Physical and computational domain of a cut-cell grid with hypersonic flow over a blunt body with surface roughness: (a) physical grid, (b) computational grid with a transformed roughness.

Please cite this article in press as: Fong KD et al. Numerical simulation of roughness effect on the stability of a hypersonic boundary layer. Comput Fluids (2014), http://dx.doi.org/10.1016/j.compfluid.2014.01.009

steady and unsteady flows with surface roughness are considered. The free stream conditions are the same as those used in Maslovs experiment [6] as follows,

$$\begin{cases} P_r = 0.72, \quad R_\infty = \rho_\infty * u_\infty/\mu_\infty = 13.2 \times 10^6/\text{m} \\ M_\infty = 5.92, \quad T_\infty = 48.69\ \text{K}, \quad P_\infty = 742.76\ \text{Pa} \end{cases}$$

where M_∞, T_∞, P_∞, P_r, R_∞ are Mach number, freestream temperature, freestream pressure, Prandtl number and unit Reynolds number, respectively. The flat plate is assumed to be isothermal. An isolated roughness element of smooth shape is placed on the surface of the flat plate. Motivated by Whitehead's experiments [21], the shape of the surface roughness is chosen to be a two-dimensional bump, governed by the elliptic equation,

$$\frac{(x - x_r)^2}{a^2} + \frac{y^2}{b^2} = h^2$$

where the parameters a, b, and h control roughness width and height. In current test cases, the roughness width is fixed at 2 times the local boundary layer thickness while the height ranges from 25% to 62.5% of the local boundary layer thickness. In addition, x_r defines the location of the roughness center. The grid size is 241 points in the stream-wise direction and 121 points in the wall-normal direction in each computational zone. The third-order cut-cell method is used to compute the two-dimensional viscous hypersonic flow over the flat plate with the roughness element.

4.2. Steady flow solution with single surface roughness element

As mentioned previously in Section 4.1, the high order cut-cell method is implemented to model the roughness. In order to study the effect of both roughness location and roughness height on a hypersonic flat plate boundary layer, the roughness is placed at four different locations. For each location, four different roughness heights ranging from 25% to 62.5% of the local boundary layer thickness are considered. The roughness location is chosen according to the synchronization point of Mode S at 100 kHz that will be imposed onto the flow for unsteady simulations. For this case, the synchronization point is located at, $x_s = 0.331$ m. The details of the synchronization point will be discussed in Section 4.4. The settings for each cases are:

Case 1: Roughness far upstream of the synchronization point. $x_r = 0.1101$ m; Local boundary layer thickness, $\delta = 1.448 \times 10^{-3}$ m; roughness height 0.25δ, 0.375δ, 0.5δ, 0.625δ.

Case 2: Roughness upstream of the synchronization point. $x_r = 0.185$ m; Local boundary layer thickness, $\delta = 1.61 \times 10^{-3}$ m; roughness height 0.25δ, 0.375δ, 0.5δ, 0.625δ.

Case 3: Roughness at the synchronization point. $x_r = 0.331$ m; Local boundary layer thickness, $\delta = 2.82 \times 10^{-3}$ m; roughness height 0.25δ, 0.375δ, 0.5δ, 0.625δ.

Case 4: Roughness downstream of the synchronization point. $x_r = 0.410$ m; Local boundary layer thickness, $\delta = 3.42 \times 10^{-3}$ m; roughness height 0.25δ, 0.375δ, 0.5δ, 0.625δ.

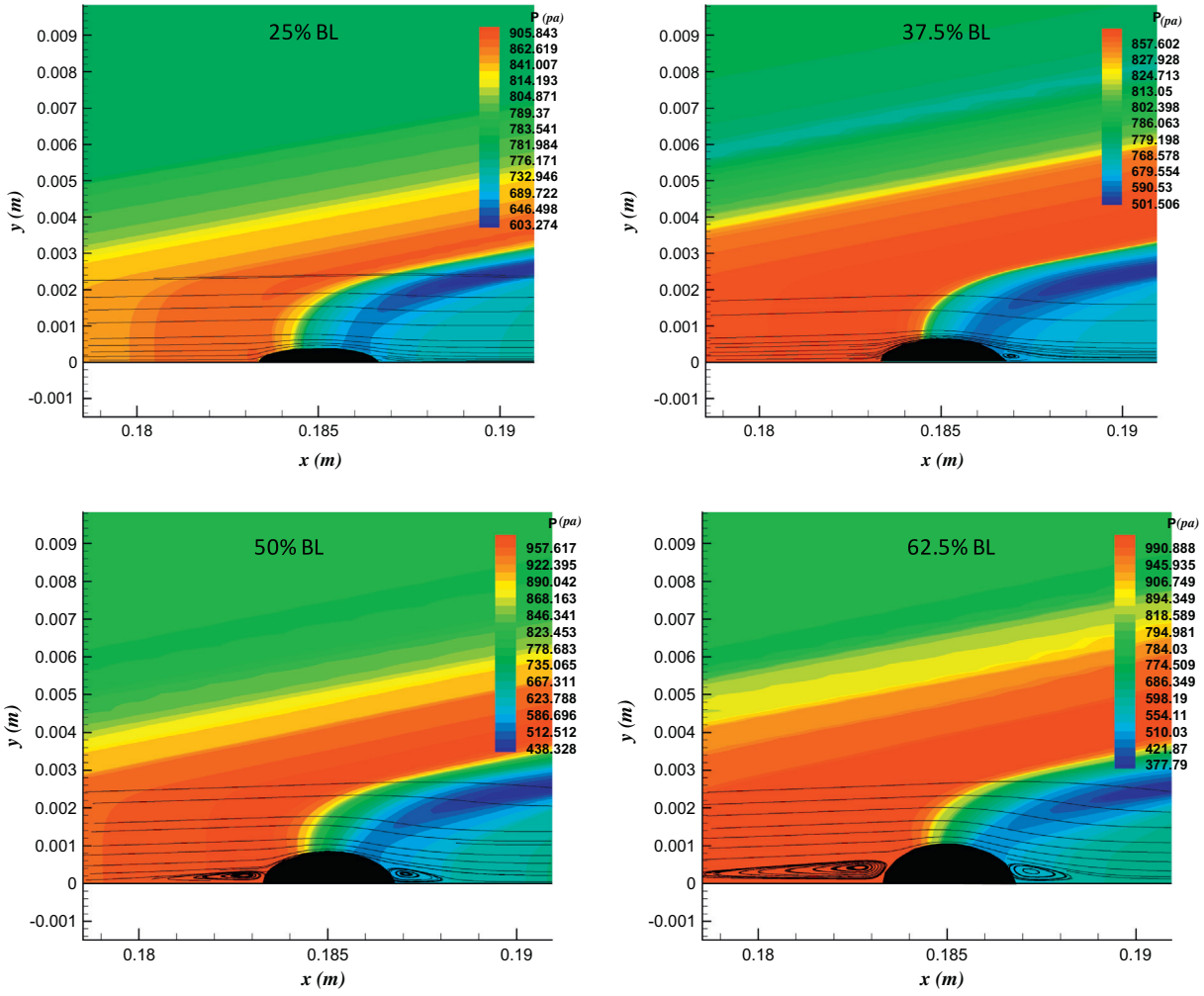

Fig. 3. Pressure contours and streamline pattern around different roughness types.

Please cite this article in press as: Fong KD et al. Numerical simulation of roughness effect on the stability of a hypersonic boundary layer. Comput Fluids (2014), http://dx.doi.org/10.1016/j.compfluid.2014.01.009

Fig. 2 shows the schematic of the current numerical simulation. The hypersonic flow is traveling from left to right at Mach 5.92. As the flow hits the flat-plate, an oblique shock and a hypersonic boundary layer are generated above it. For simulations with roughness, a roughness element is mounted on the surface of the flat plate for each test cases. Pure Mode S or a wall normal velocity pulse is imposed in the far upstream region to disturb the flow. Fig. 3 shows the pressure contour and streamline pattern for case 2 in which the roughness is located at $x_r = 0.185$ m. A strong compression region is observed upstream of the roughness. Around the roughness, Mach waves are generated, and they travel downstream at an angle almost parallel to the shock. In the downstream vicinity of the roughness, expansion waves can be seen. Moreover, the streamline pattern shows that roughness introduces circulation around itself. As Fig. 3 shows, the size of the circulation region is bigger upstream of the roughness. Bigger roughness also results in a bigger circulation. A Mach number contour is shown in Fig. 4. It shows that roughness increases the Mach number boundary layer.

Similar to the paper by Klebanoff [22], we are interested in the region upstream and downstream of a roughness element where the flow is distorted by the existence of the roughness. Figs. 5 and 6 show the stream wise velocity profile upstream of the roughness for case 2 with roughness heights of 25% and 62.5% of the local boundary layer thickness at different stream wise locations. The symbols in the figure represent the velocity profile for the case with roughness, while lines represent the profile for a flat plate without roughness. The figures clearly show that a bigger roughness not only increases the boundary layer thickness, but also extends the size of the region where the flow can feel the existence of roughness. For example, the tall roughness can affect the flow upstream at $x = 0.1446$ m, while the short roughness can only have an effect up to $x = 0.1671$ m. The same trend is observed downstream of the roughness as shown in Figs. 7 and 8. For the shortest roughness case, the distortion is weak. The recovery zone only extends to $x = 0.21683$ m. As the roughness gets larger, the distortion gets stronger and the separation region becomes more pronounced. The size of the recovery zone consequentially becomes bigger. In our tallest roughness case, the recovery zone extends to $x = 0.24135$ m.

4.3. Grid independence study for steady flow solution

A grid independence study is performed to validate our numerical results for the steady flow. In particular, the grid study is done on case 2 in which the roughness is located at $x_r = 0.185$ m with a roughness height of 50% of the local boundary layer thickness. A double grid in the x-direction simulation and a double grid in the y-direction simulation are performed independently to save computational time. Fig. 9 shows the stream wise velocity and wall normal velocity at $x = 0.186$ m for the regular grid and the double

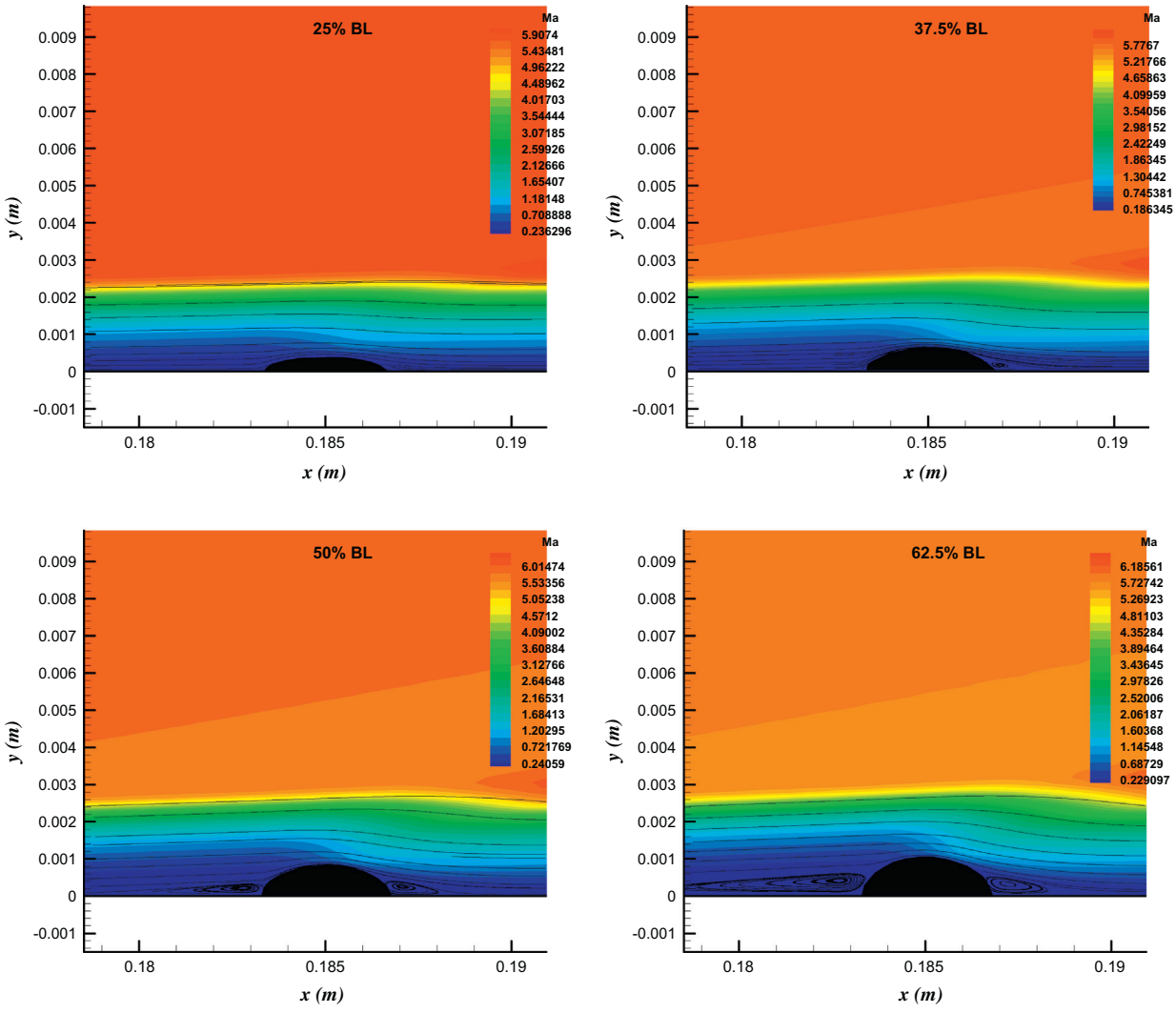

Fig. 4. Mach number contours and streamline pattern around different roughness types.

Please cite this article in press as: Fong KD et al. Numerical simulation of roughness effect on the stability of a hypersonic boundary layer. Comput Fluids (2014), http://dx.doi.org/10.1016/j.compfluid.2014.01.009

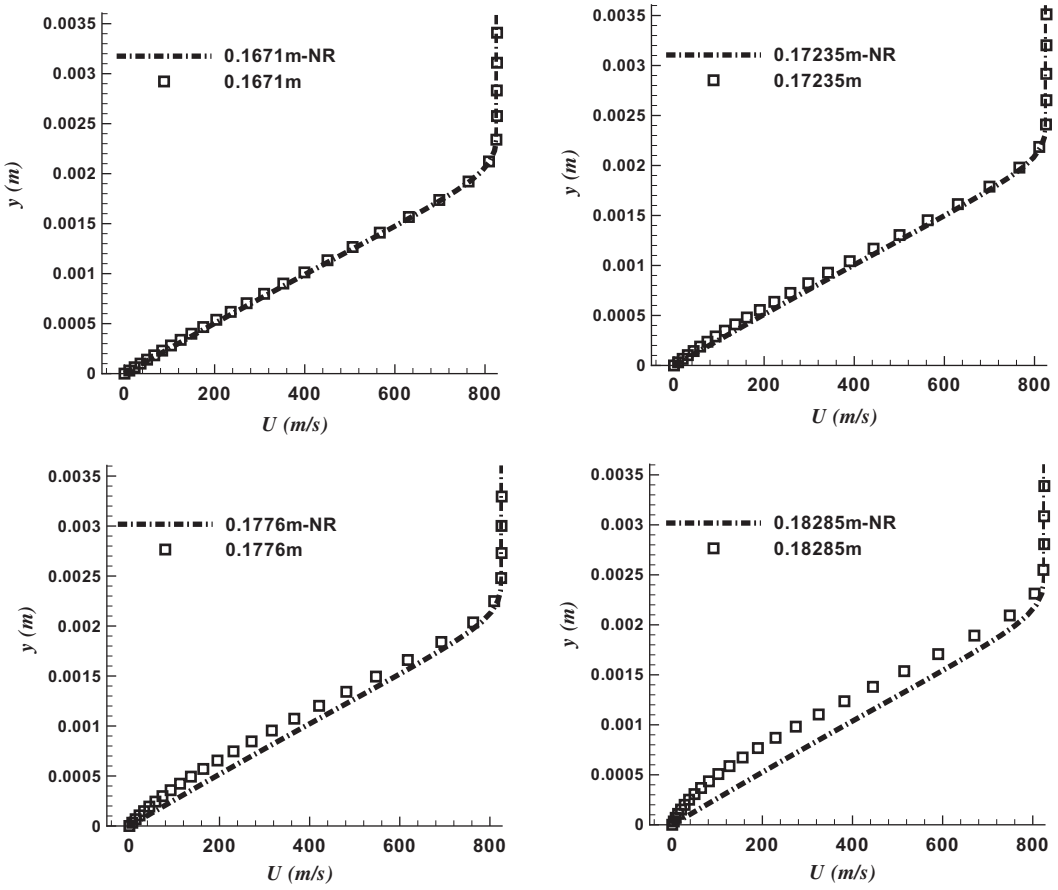

Fig. 5. Stream wise velocity profile at different locations upstream of the 25% roughness compared with the no roughness case.

grid in the x-direction. This location is chosen because it is near the roughness element and a separation bubble can been seen (the negative stream wise velocity in the near wall region). Therefore, this location is sensitive to grid changes, and can be used as a benchmark for grid dependence. The good agreement shown in Fig. 9 suggests that the regular grid is grid independent in the x-direction. On the other hand, Fig. 10 shows the stream wise velocity and wall normal velocity for the regular grid and the double grid in the y-direction taken at the same location. It is seen that the two grids agree well. From the results, it is concluded that the regular grid is grid independent in both x and y directions.

4.4. Stability characteristics of boundary layer without roughness

The stability characteristics of boundary layer waves for the Mach 5.92 flow over a flat plate is studied by LST using a multi-domain spectral method defined in Malik et al. [23]. The dimensionless frequency used for linear stability analysis is defined as

$$F = \frac{2\pi f \nu}{u_\infty^2} \tag{12}$$

where F is the dimensionless frequency and ν is kinematic viscous coefficient. In present simulations, $\mu = 6.05 \times 10^{-5}$ m^2/s and $F = 5.30 \times 10^{-5}$ for f = 100 kHz and $u_\infty = 827.29$ m/s.

In LST analyses of boundary layer flows, the Reynolds number is based on the local length scale of the boundary layer thickness δ. They are expressed as

$$R = \frac{\rho_\infty u_\infty \delta}{\mu_\infty}, \quad \delta = \sqrt{\frac{\mu_\infty x}{\rho_\infty u_\infty}} \tag{13}$$

Hence the relation between R and the unit Reynolds number R_∞ is

$$R = \sqrt{R_\infty x} \tag{14}$$

With the definitions of Reynolds number R and the dimensionless frequency F, the dimensionless circular frequency, ω, can be expressed as,

$$\omega = RF \tag{15}$$

Fig. 11 shows the eigenvalue spectra of boundary-layer waves at a frequency of 100 kHz at $x = 0.189$ m. The figure shows wave spectra corresponding to the fast acoustic wave, entropy and vorticity waves, and the slow acoustic wave. The two discrete waves marked by circles are Modes F and S, respectively. Mode F originates from the fast acoustic spectrum on the left side of the figure and passes the entropy and vorticity spectra at the center as the dimensionless frequency increases. Mode S originates from the slow acoustic spectrum on the right side of the figure. It becomes unstable in a certain range of dimensionless frequencies. The figure also shows that Mode S at this frequency is unstable at $x = 0.189$ m with $\alpha_i < 0$.

Fig. 12 shows phase velocities of boundary layer waves at two locations where $x = 0.159$ m and $x = 0.189$ m as a function of circular frequency. The three horizontal dashed lines represent phase velocities of the fast acoustic wave, entropy and vorticity waves, and the slow acoustic wave, respectively. The excellent agreement of phase velocities at two different locations indicates that phase velocity is approximately a function of circular frequency only. The figure clearly shows that Mode F originates from the fast acoustic spectrum. As ω increases, the phase velocity of Mode F decreases. When Mode F passes the entropy and vorticity spectra

Please cite this article in press as: Fong KD et al. Numerical simulation of roughness effect on the stability of a hypersonic boundary layer. Comput Fluids (2014), http://dx.doi.org/10.1016/j.compfluid.2014.01.009

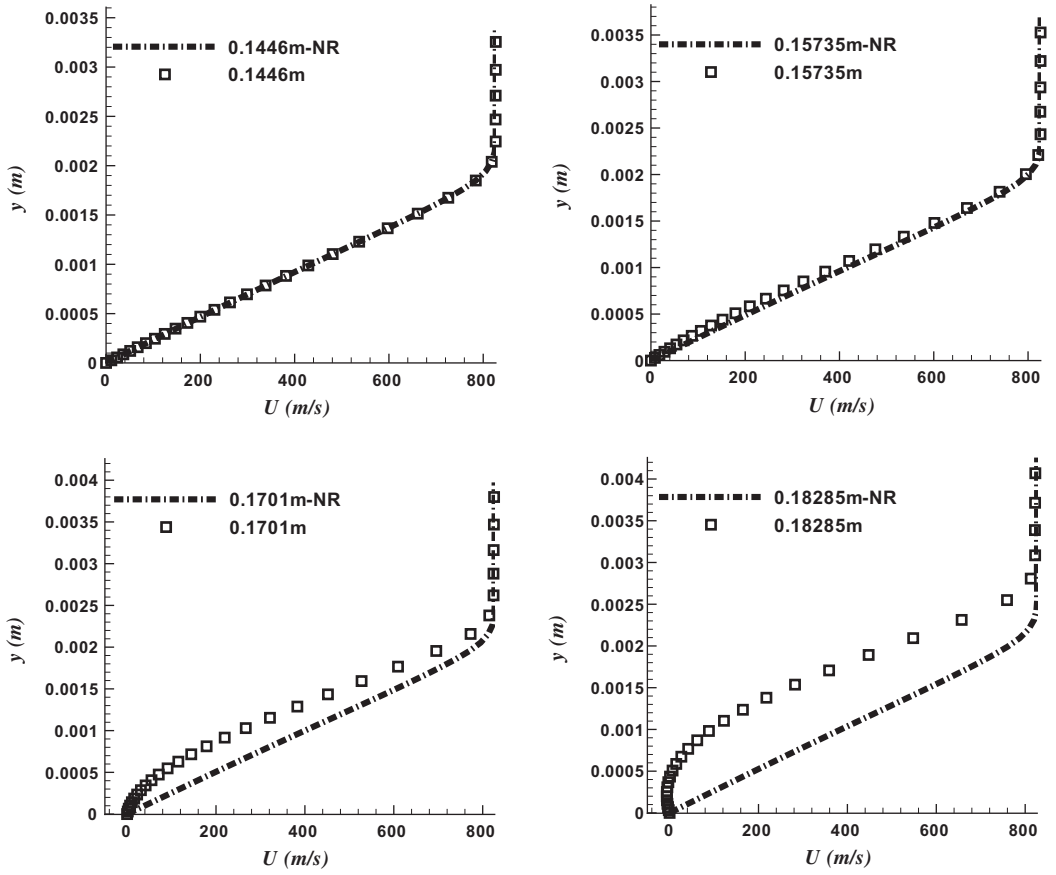

Fig. 6. Stream wise velocity profile at different locations upstream of the 62.5% roughness compared with the no roughness case.

near $\omega = 0.1$, there exists a jump of phase velocity which is consistent with theoretical analysis of Fedorov and Khokhlov [24]. On the other hand, Mode S originates from the slow acoustic spectrum. The figure also shows that Mode S synchronizes with Mode F at the point where $\omega_s = 0.11563$ and $a_s = 0.93076$.

Although Fig. 12 shows that the synchronization point has a constant value of non-dimensional circular frequency $\omega_s = 0.11563$, the dimensional location of the synchronization point in the x coordinate, x_s, is different for different dimensionless frequencies F. The synchronization location in the x coordinate for a given dimensionless frequency can be calculated from

$$x_s = \frac{(\omega_s/F)^2}{\mathrm{Re}_\infty} \tag{16}$$

This equation indicates that the synchronization point moves upstream with increasing dimensionless frequency. Fig. 13 shows growth rates of modes F and S at the same set of locations as a function of circular frequency. The horizontal dotted line represents neutral waves when $\alpha_i = 0$. A mode is unstable when $\alpha_i < 0$. In Fig. 13, the growth rates of both Mode S and Mode F are approximately functions of circular frequency only. Mode S is unstable in the region from $\omega_I = 0.000827$ to $\omega_{II} = 0.18465$, whereas Mode F is always stable. The parameters ω_I and ω_{II} are called branch I and II neutral points of mode S. The locations of branch I and II neutral points in the x coordinate change with different dimensionless frequencies. They can be calculated by

$$x_I = \frac{(\omega_I/F)^2}{\mathrm{Re}_\infty}, \quad x_{II} = \frac{(\omega_{II}/F)^2}{\mathrm{Re}_\infty} \tag{17}$$

which indicates that when the non-dimensionalized frequency (F) increases, the corresponding coordinates of the branch points decrease. In other words, branches I and II neutral points move upstream when F increases. For a disturbance at $F = 100$ kHz, the branch I and branch II neutral points are located at 0.00678977 m and 3.384887 m. More results on the LST analysis on the mean flow without roughness can be found in Wang and Zhongs paper [25].

4.5. The effect of a single roughness element of different heights on Mode S

From LST, the eigenfunction of the Mode S perturbation is found and is imposed onto the mean flow with and without surface roughness. Moreover, FFT analysis is performed on the unsteady simulations to study the evolution of the perturbation in the stream wise direction. Figs. 14(a) and (b) show the growth of the Mode S pressure perturbation on the wall for case 1 and case 2 respectively. The results for each roughness height are also included in each plots. The symbol h on the figures represents the local boundary layer thickness. Since the cut-cell method does not solve for the grid points inside the solid region, all perturbations drop back to zero inside the roughness element. This is what causes the discontinuity in the plots. The roughness element of case 1 and case 2 are located upstream of the synchronization point at $x_r = 0.1101$ m and $x_r = 0.185$ m respectively. In Fig. 14(a), it is seen that the perturbation for the 37.5% roughness is damped slightly in front of the roughness before it starts to grow. The physical explanation for this is not known. However, for all other roughness heights, roughness upstream of the synchronization point always amplifies perturbations upstream of the roughness. The amplification rate depends strongly on the size of roughness. For example, in case 2, the 25% roughness element has the maximum amplitude just about three times the case

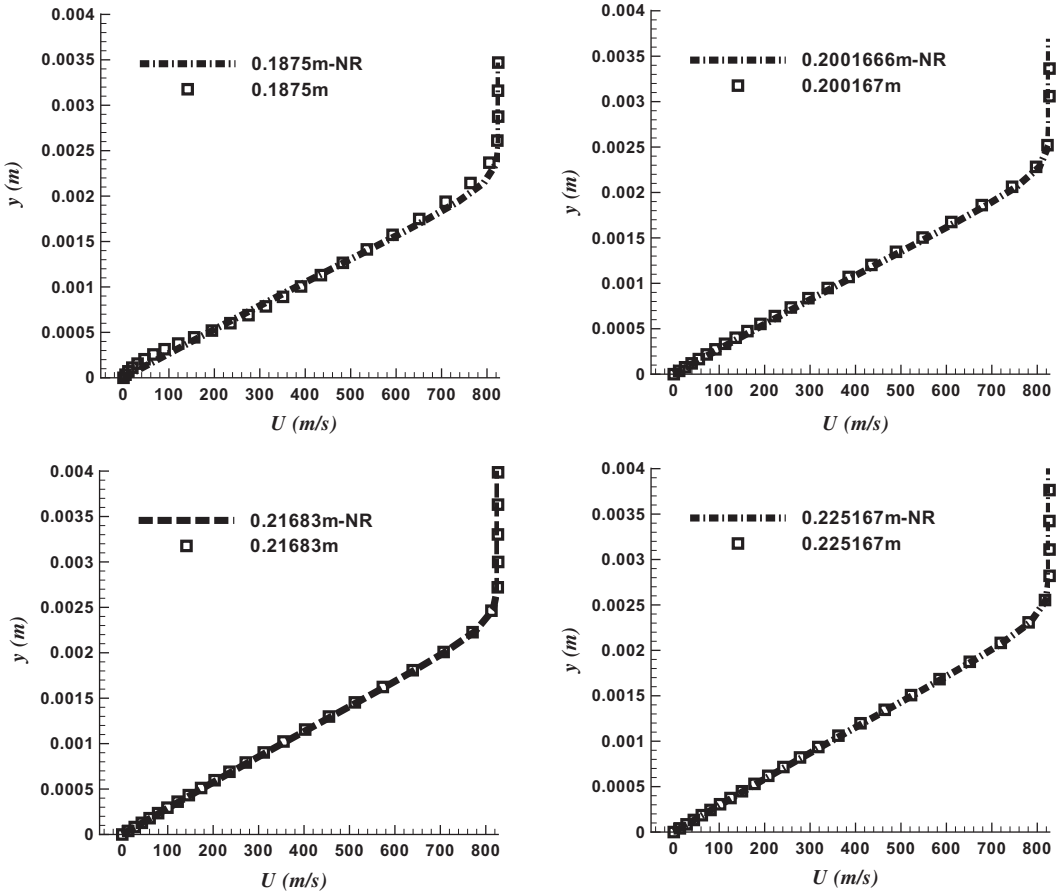

Fig. 7. Stream wise velocity profile at different locations downstream of the 25% roughness compared with the no roughness case.

without roughness. However, in the tallest roughness case, the perturbation amplitude reaches as high as thirteen times that without roughness. This amplification in the separation region upstream of the roughness agrees with the results of Marxen et al. [26].

Downstream of the roughness, the perturbation evolution has different trends depending on the roughness location. In case 1, perturbation stays at the same level as the no roughness case. However, in case 2 (Fig. 14(b)), the roughness height controls how the perturbation grows downstream. It is found that perturbations are amplified for tall roughness (50% and 62.5%). For small roughness, perturbations remain the same as no roughness. In general, a roughness element at this location has a more pronounced amplification effect in the vicinity upstream of the roughness rather than downstream. Moreover, if roughness is placed too upstream of the synchronization point, it tends to have a very small effect on modal growth. If a roughness element is placed a little bit downstream, the overall effect of the roughness is to amplify perturbations.

As the roughness moves closer to the synchronization point in case 3 and case 4, the roughness effect is completely different. In Fig. 14(c), the roughness sits at exactly the synchronization point of the perturbation frequency. The perturbation for the smallest roughness, 25%, is still amplified and grows downstream as if there is no roughness. However, for taller roughness, the perturbation only grows in the far upstream region. As the perturbation gets closer to the roughness, it is damped suddenly. The location where the damping starts depends on roughness height. In the 37.5% case, damping starts around $x = 0.317$ m. When the roughness height is increased to 50%, the onset of damping moves to $x = 0.309$ m. Further increasing the roughness height to 62.5% moves the damping even more upstream to $x = 0.303$ m. Downstream of the roughness, the perturbation in the small roughness case (25%) follows the trend of the no roughness case. On the other hand, perturbation are highly damped in the tall roughness cases. The larger the roughness is, the weaker the pressure perturbation is compared to the case without roughness. Tall roughness at the synchronization point acts as a perturbation damper of the imposed mode instead of an amplifier.

In the final test case, the roughness is moved even further downstream to $x_r = 0.410$ m which is downstream the synchronization point for the imposed frequency. Fig. 14(d) shows how the pressure perturbation interacts with different roughness heights at this location. Similar to case 3, the perturbation is amplified far upstream of the roughness, but is entirely damped when it is near the roughness. One difference between this case and case 3 is the damping effect is observed for all roughness heights. In addition, the location of the onset of damping moves further upstream than in case 3. In the region behind the roughness, perturbations for all cases stay on the same level and do not grow at all. This is significantly different from case 3. Judging from this result, it can be concluded that roughness in this location acts as a more effective perturbation damper for the imposed mode than case 3. Placing a roughness element downstream of the synchronization point can potentially stabilize the flow.

In the simulations, it is found that the relative location of a roughness element and the synchronization point has a very important effect on Mode S. Placing a roughness element upstream of the synchronization point will amplify the mode. The effect is reversed if the roughness element is placed at or downstream of the synchronization point. Moreover, roughness height also plays a

Please cite this article in press as: Fong KD et al. Numerical simulation of roughness effect on the stability of a hypersonic boundary layer. Comput Fluids (2014), http://dx.doi.org/10.1016/j.compfluid.2014.01.009

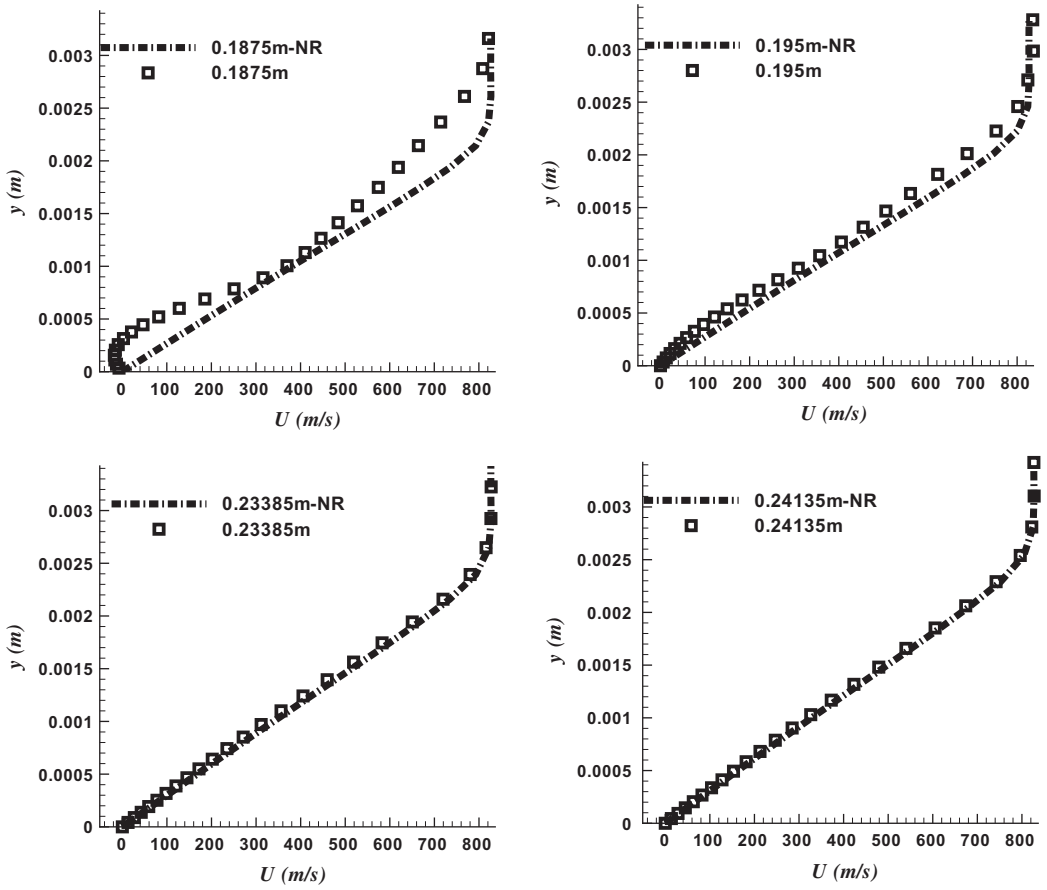

Fig. 8. Stream wise velocity profile at different locations downstream of the 62.5% roughness compared with the no roughness case.

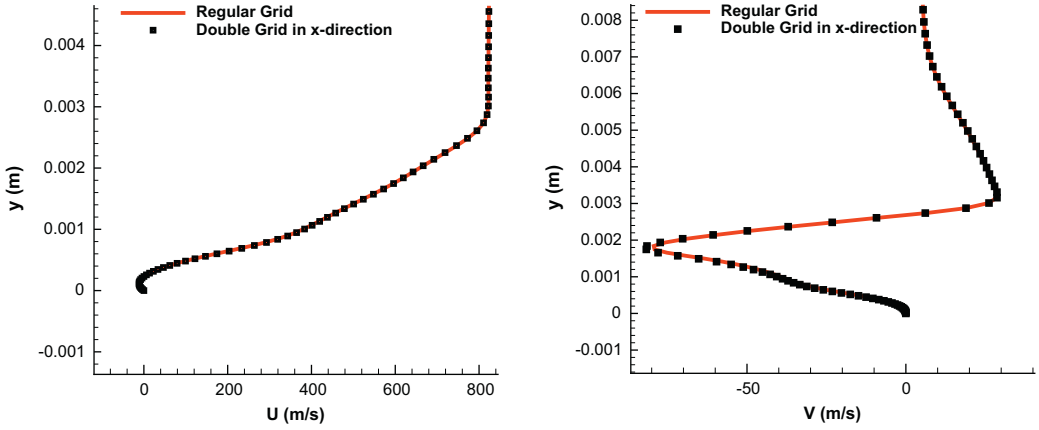

Fig. 9. Stream wise and wall normal velocity profile at $x = 0.186$ m for normal grid and double grid in x-direction.

role. It has been shown that, for a roughness element less than the local boundary thickness, taller roughness elements result stronger amplification or stronger damping depending on the roughness element location.

4.6. The effect of roughness on disturbances of different frequencies

Alternatively to investigating perturbation growth for a single frequency, it is also of interest to investigate how roughness affects perturbations at different frequencies. Ideally, a delta function can be used to produce perturbations containing the entire frequency spectrum. In present simulations, a Gaussian shape pulse perturbation is used to approximate the delta function. A hole is modeled on the flat plate located at $x_h = 0.1$ m with a width of $h = 0.003$ m. The hole introduces a wall normal velocity pulse in the mean flow according to

$$\Delta V(x,t) = \Delta V_{max} e^{\left(-\frac{t^2-\mu^2}{2\sigma^2}\right)} \sin\left(\frac{2\pi(x-x_h)}{h}\right) \tag{18}$$

where ΔV_{max} is the maximum wall normal velocity perturbation, σ and μ control the frequency range and the shape of the Gaussian perturbation, x_h is the x-coordinate of the hole center, h is the total

Please cite this article in press as: Fong KD et al. Numerical simulation of roughness effect on the stability of a hypersonic boundary layer. Comput Fluids (2014), http://dx.doi.org/10.1016/j.compfluid.2014.01.009

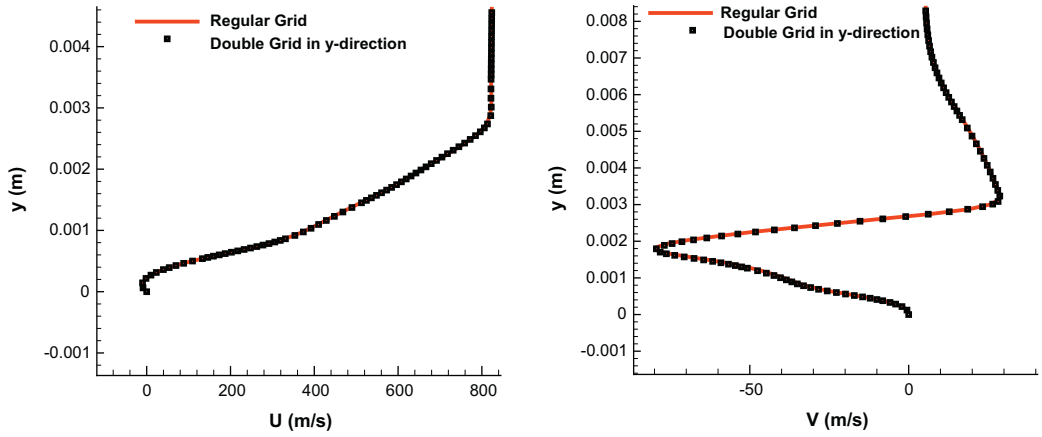

Fig. 10. Stream wise and wall normal velocity profile at $x = 0.186$ m for normal grid and double grid in y-direction.

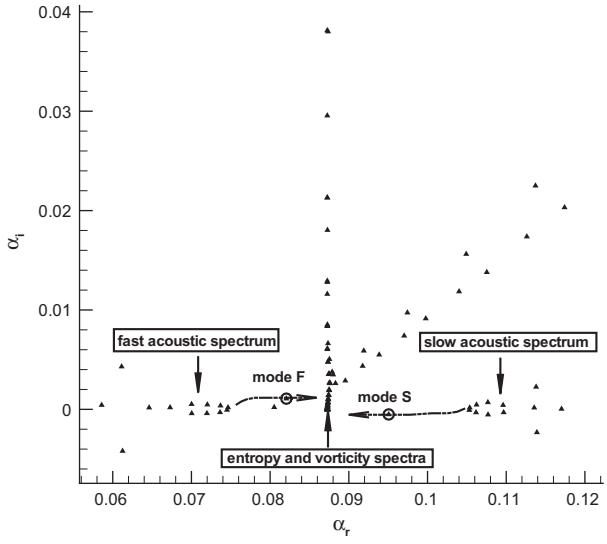

Fig. 11. Eigenvalue spectra of boundary-layer waves at the frequency of $f = 100$ kHz at $x = 0.189$ m.

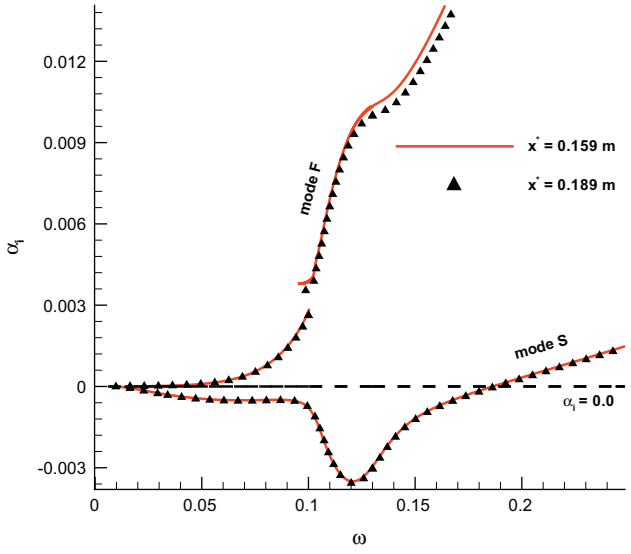

Fig. 13. Distributions of growth rates of modes F and S at two different locations.

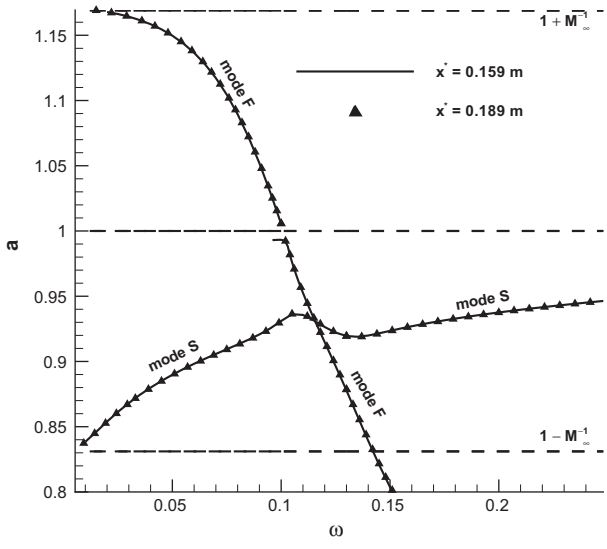

Fig. 12. Distributions of phase velocities for boundary-layer waves at two different locations.

length of the hole. The sinusoidal part in Eq. (18) is to ensure no additional mass is added.

Fig. 15(a) and (b) show the perturbation pulse in time and space respectively. Since the velocity pulse is weak, the forcing wave in the form of a pulse is the same as simultaneously forcing a combination of different frequencies. For example,

$$\Delta V(x,t) = \sin\left(\frac{2\pi(x-x_h)}{h}\right)\sum_{n=1}^{\infty}\Delta V_n \sin(2\pi f_n t + \phi_n) \qquad (19)$$

where ΔV_n and ϕ_n denote the perturbation amplitude and phase angle at frequency f_n. Fig. 15(c) shows the frequency spectrum of the Gaussian perturbation obtained from a FFT. It is seen that the frequency range is about 1 MHz before the amplitude drops very close to zero. This frequency range adequately covers all unstable modes in the boundary layer for this particular flow condition.

This pulse model is implemented into the mean flow of case 2 where the roughness is located at $x_r = 0.185$ m with a height 50% of the local boundary layer thickness. Fig. 16 shows the pressure perturbation contour resulting from the pulse. The hole and the roughness are also shown in the figure. Fig. 17 shows the instantaneous pressure perturbation at different locations. It is seen that besides the excited perturbation on the wall region, the wall normal velocity pulse has excited a perturbation outside of the

Please cite this article in press as: Fong KD et al. Numerical simulation of roughness effect on the stability of a hypersonic boundary layer. Comput Fluids (2014), http://dx.doi.org/10.1016/j.compfluid.2014.01.009

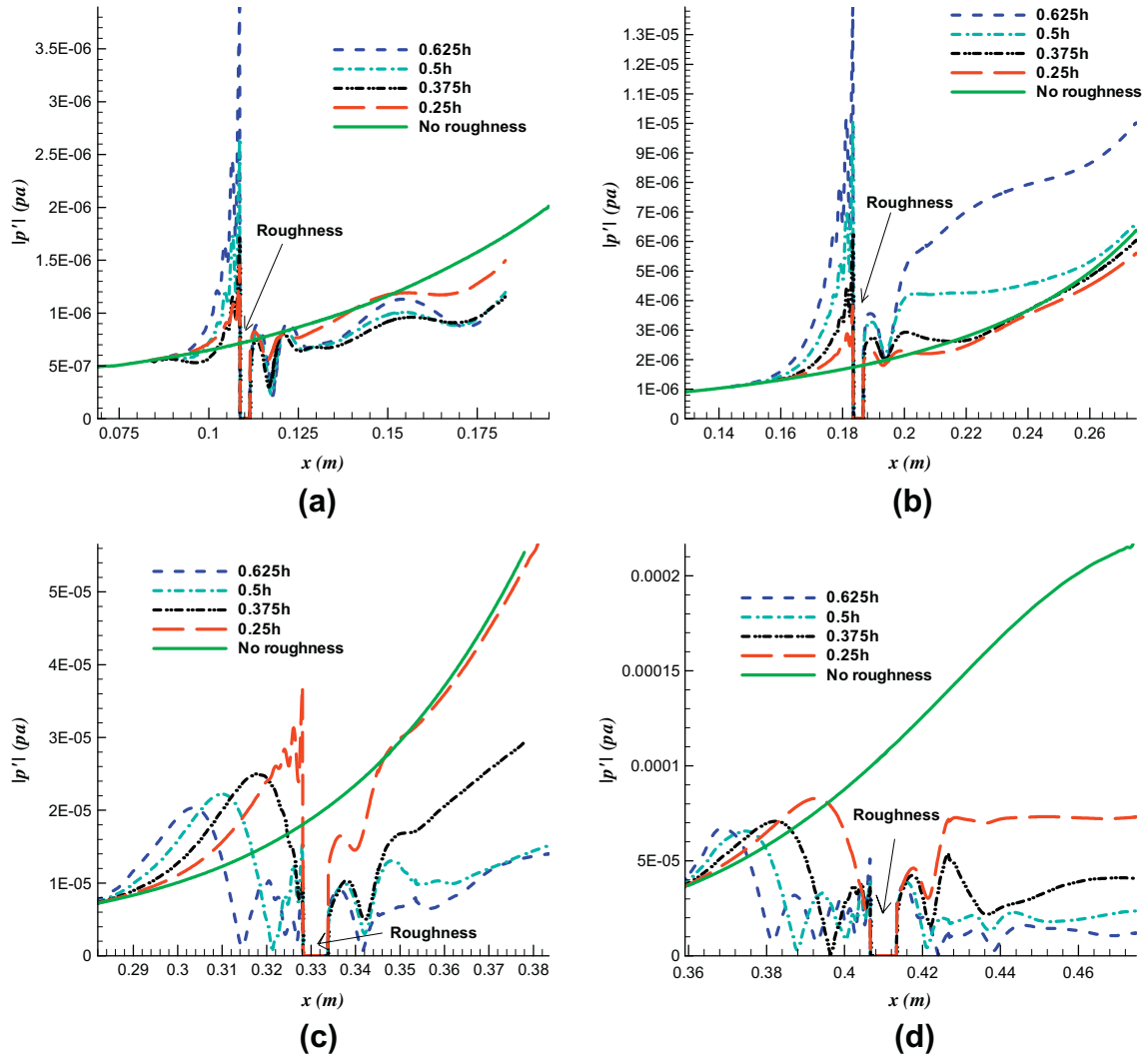

Fig. 14. Evolution of Mode S wall pressure perturbations with different roughness heights: (a) case1 roughness at $x = 0.1101$ m; (b) case 2 roughness at 0.185 m; (c) case 3 roughness at 0.331 m; (d) case 4 roughness at 0.410 m.

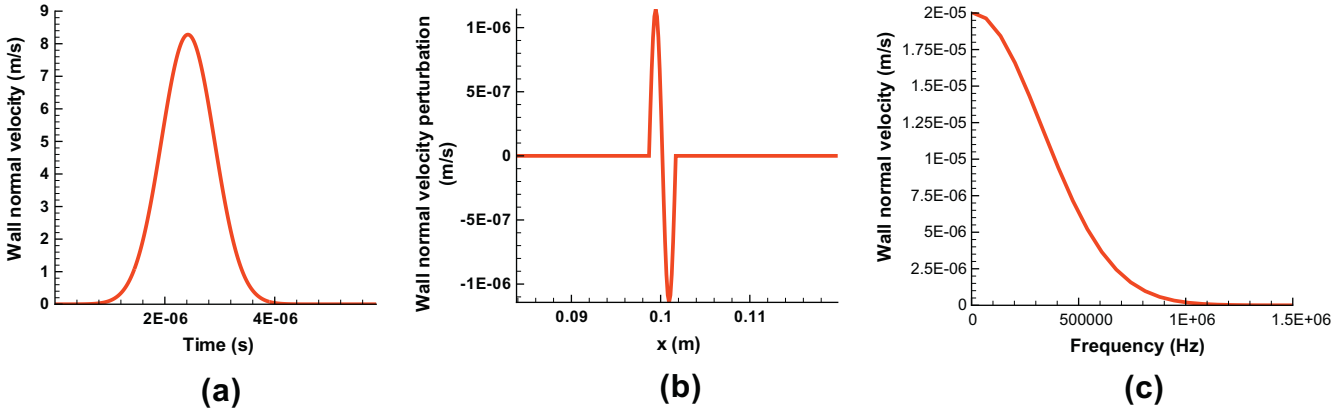

Fig. 15. (a) Time history of wall normal velocity on the wall. (b) Snapshot of wall normal velocity in space. (c) FFT result of the Gaussian shape perturbation in (a).

boundary layer. However, this perturbation is weak and it decays quickly outside of the boundary layer. The pulse also excites modes in the boundary layer and creates a pressure perturbation on the wall with a pattern similar to Mode S. However, this perturbation is not periodic due to the Gaussian nature of the pulse.

Fig. 18 shows the time history of wall pressure perturbations at various stream wise locations upstream of the roughness. Initially, the front part of the wave packet is amplified as it travels closer to the roughness, while the tail is slightly damped. When the wave packet travels further, for example at 0.18285 m, the front is also

Please cite this article in press as: Fong KD et al. Numerical simulation of roughness effect on the stability of a hypersonic boundary layer. Comput Fluids (2014), http://dx.doi.org/10.1016/j.compfluid.2014.01.009

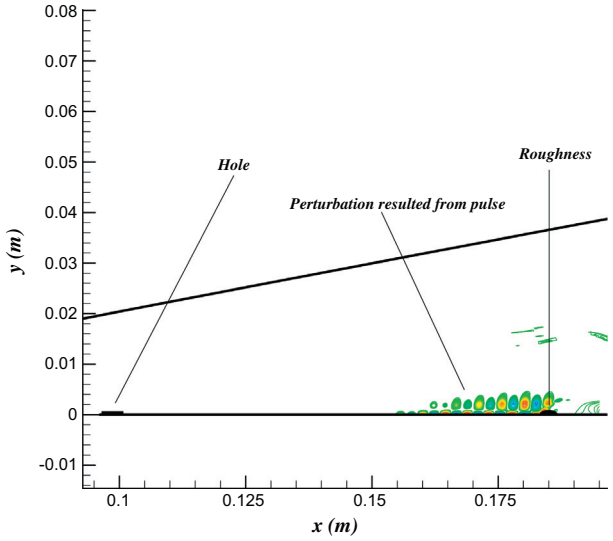

Fig. 16. Schematic presentation of numerical setup for the pulse case. The hole to introduce perturbation, roughness and pressure perturbation are shown.

damped while the tail part is highly damped. Since this pulse comprises a wide range of frequencies, an FFT analysis is used to decompose the perturbation to obtain a better understanding of the relation between roughness and perturbation frequency. Fig. 19 shows the frequency spectra of the pulse at the same locations as Fig. 18. The results for both with roughness and without roughness are included. The location of roughness in this case, $x_r = 0.185$ m, corresponds to the location of the synchronization point for a perturbation at a frequency of 133.26 kHz, which is highlighted in Fig. 19(a). It is seen that in the upstream region of the roughness, perturbations at frequencies from 0 to 120 kHz are amplified compared with the no roughness case. Moreover, the peak observed in Fig. 19(b) around 165 kHz has switched to a lower frequency region to around 129 kHz. This shift can be explained by the increase of boundary layer thickness due to the existence of roughness. Since the wavelength of the second mode is related to the boundary layer thickness, a thicker boundary layer produces a longer second mode wavelength and thus the frequency becomes lower. This result also agrees with Marxen et al. [26] in which they state that roughness can move the second mode instability to a lower frequency region. At $x = 0.18285$ m, the perturbation arrives at a location just upstream of the roughness. It can be seen that the perturbations at frequencies around 133.26 kHz are strongly damped. The lowest part of the FFT result is at 140 kHz, which is very close to the synchronization frequency.

Fig. 20 shows the time history of wall perturbations at different x locations downstream of the roughness. The front part of the wave starts to grow again once it has passed the roughness. However, the tail still exhibits some damping effect. At $x = 0.21735$ m, the tail part of the wave has reached its lowest amplitude and starts to grow thereafter. The growth at the tail has become stronger than the front after it has reached its minimum. A detailed FFT analysis on such a perturbation is shown in Fig. 21(a). Fig. 21(b) shows the FFT results of the same locations without roughness. At $x = 0.19635$ m, a location just behind the roughness, perturbations at frequencies around 100 kHz to 120 kHz are amplified

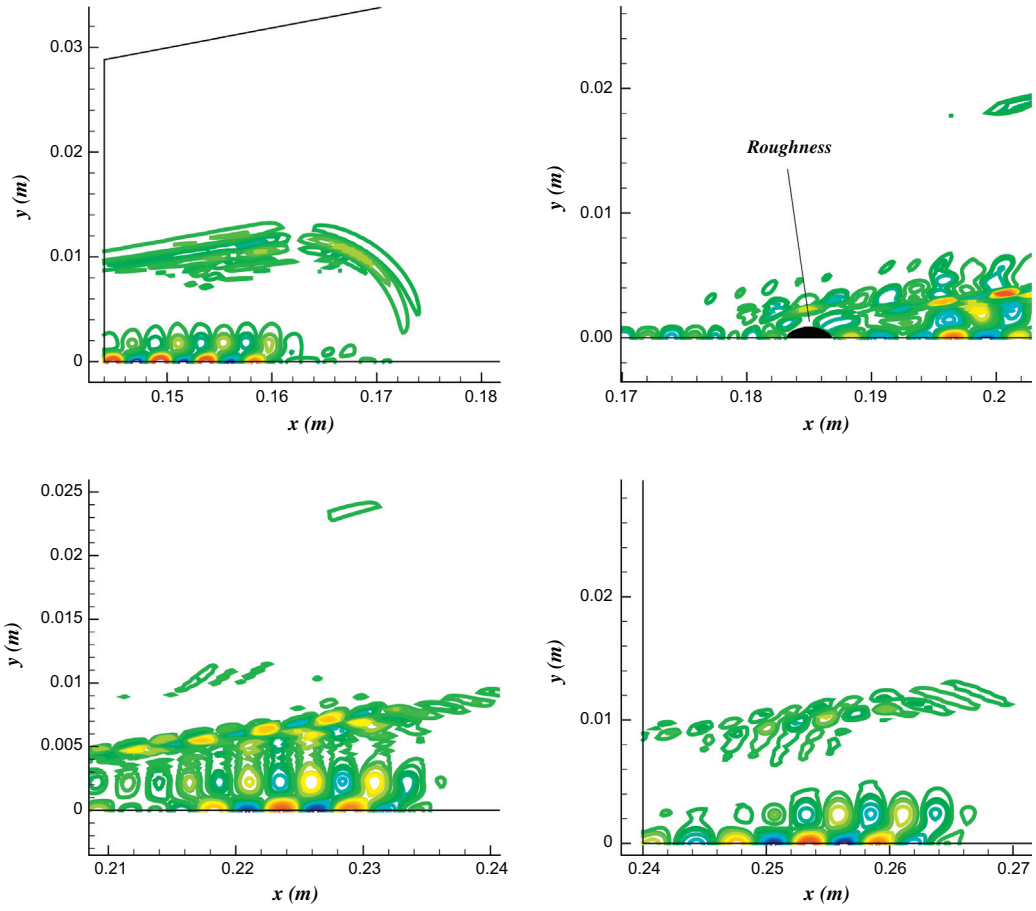

Fig. 17. Pressure perturbation contour at different locations.

Please cite this article in press as: Fong KD et al. Numerical simulation of roughness effect on the stability of a hypersonic boundary layer. Comput Fluids (2014), http://dx.doi.org/10.1016/j.compfluid.2014.01.009

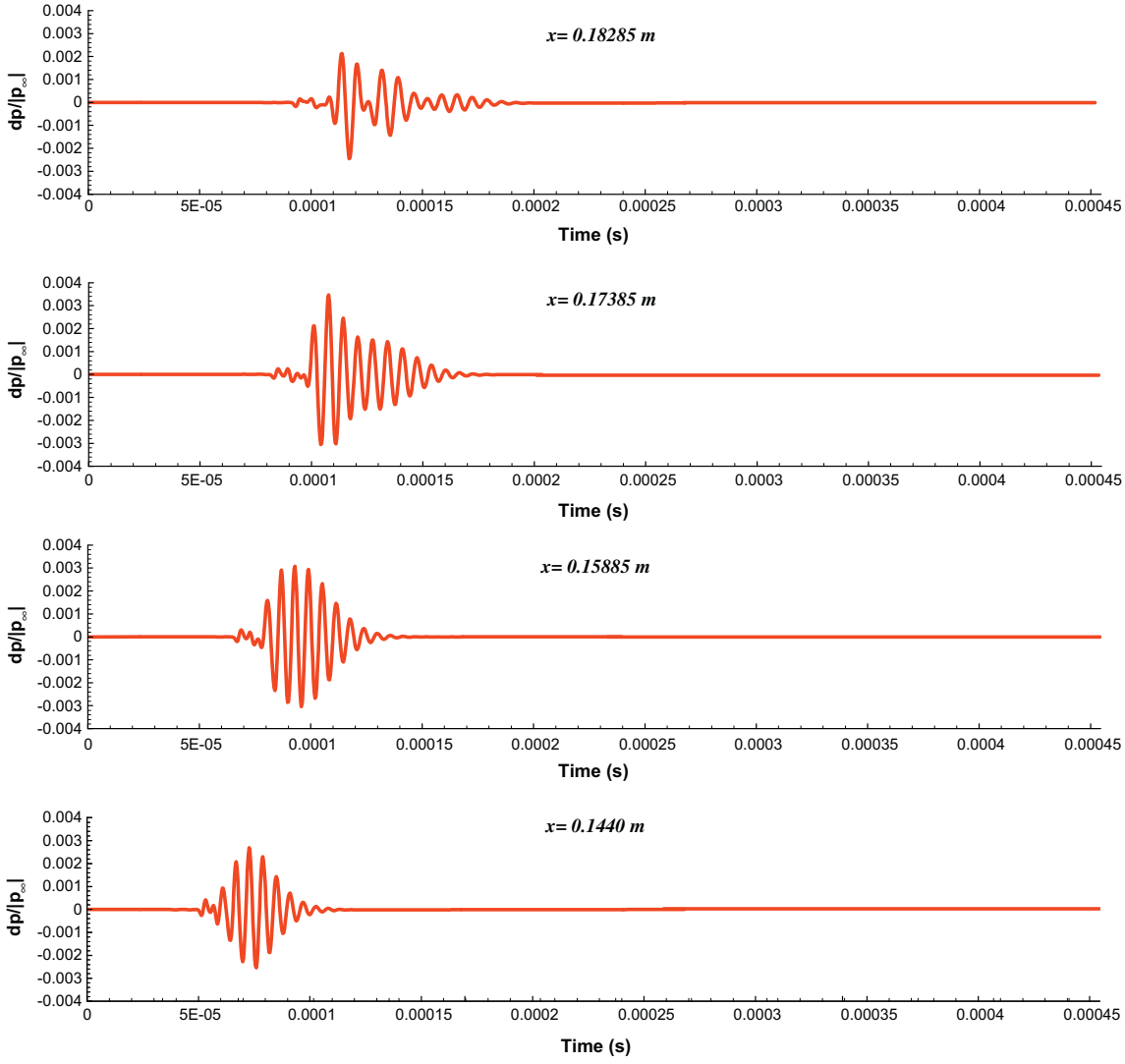

Fig. 18. Time history trace of wall pressure perturbations at various streamwise locations upstream part of the roughness.

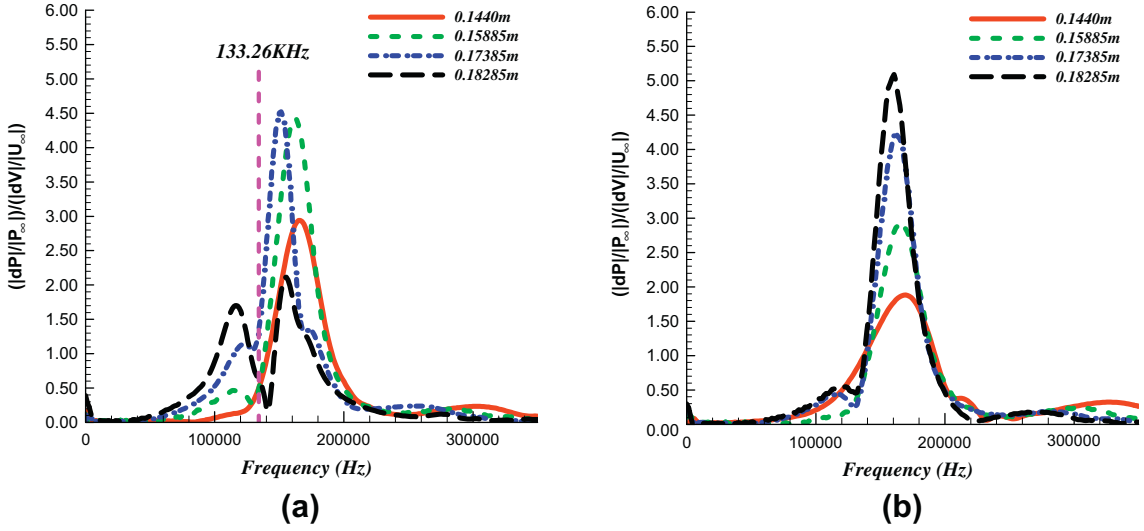

Fig. 19. Non-dimensional frequency spectra of wall pressure perturbation at different locations. (a) Upstream of roughness. (b) No roughness case.

Please cite this article in press as: Fong KD et al. Numerical simulation of roughness effect on the stability of a hypersonic boundary layer. Comput Fluids (2014), http://dx.doi.org/10.1016/j.compfluid.2014.01.009

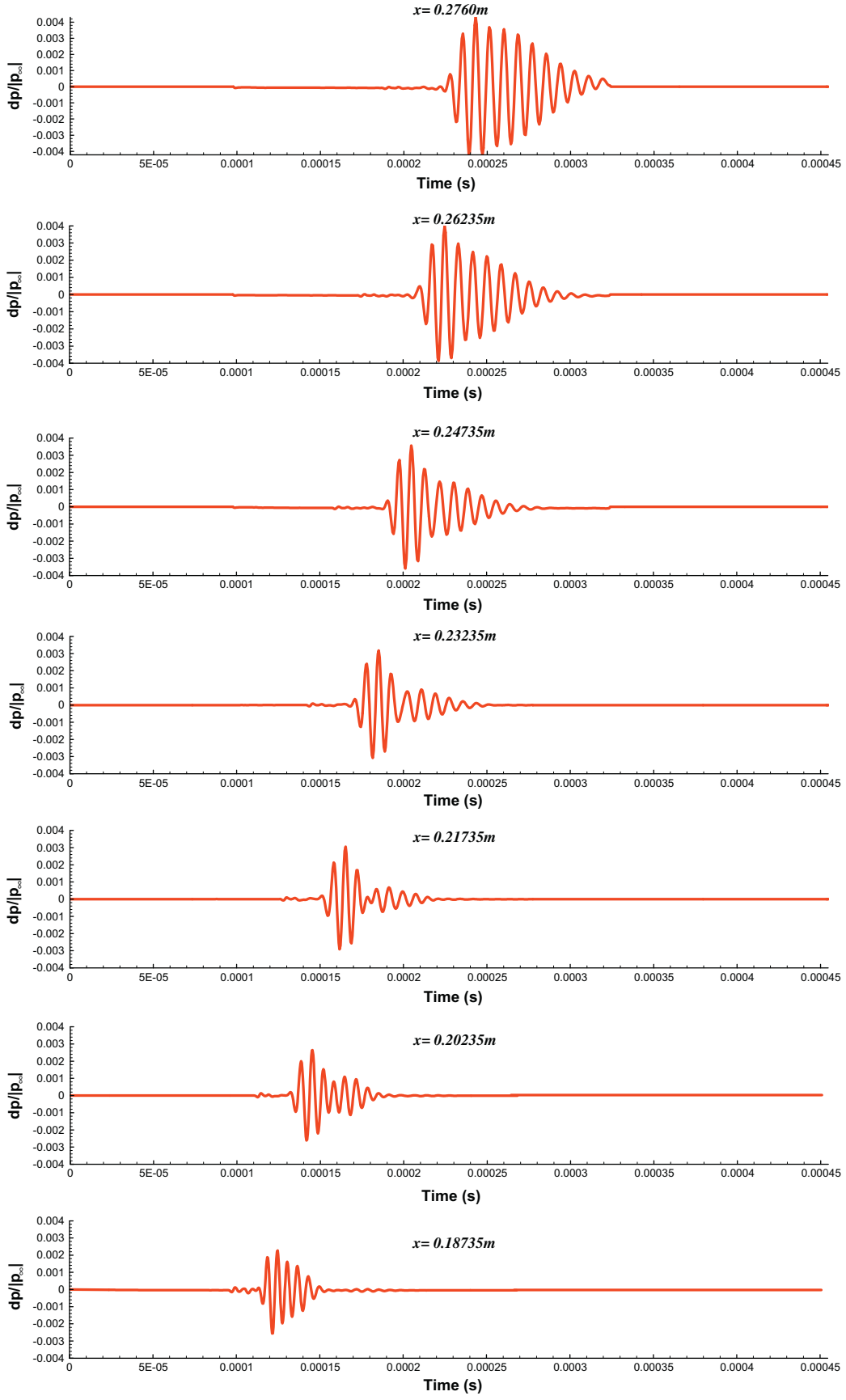

Fig. 20. Time history trace of wall pressure perturbations at various streamwise locations downstream of the roughness.

Please cite this article in press as: Fong KD et al. Numerical simulation of roughness effect on the stability of a hypersonic boundary layer. Comput Fluids (2014), http://dx.doi.org/10.1016/j.compfluid.2014.01.009

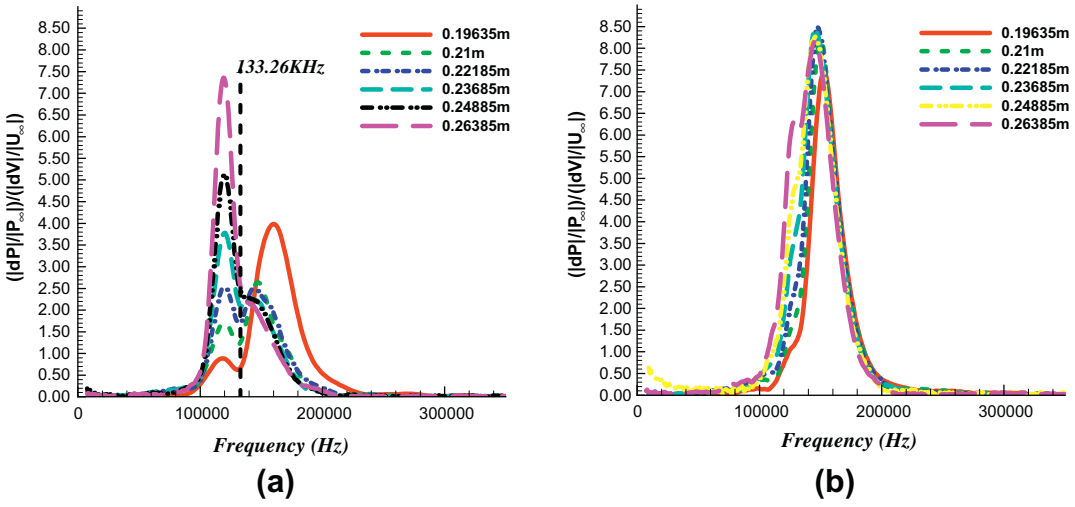

Fig. 21. Non-dimensional frequency spectra of wall pressure perturbation at different locations. (a) Downstream of roughness. (b) No roughness case.

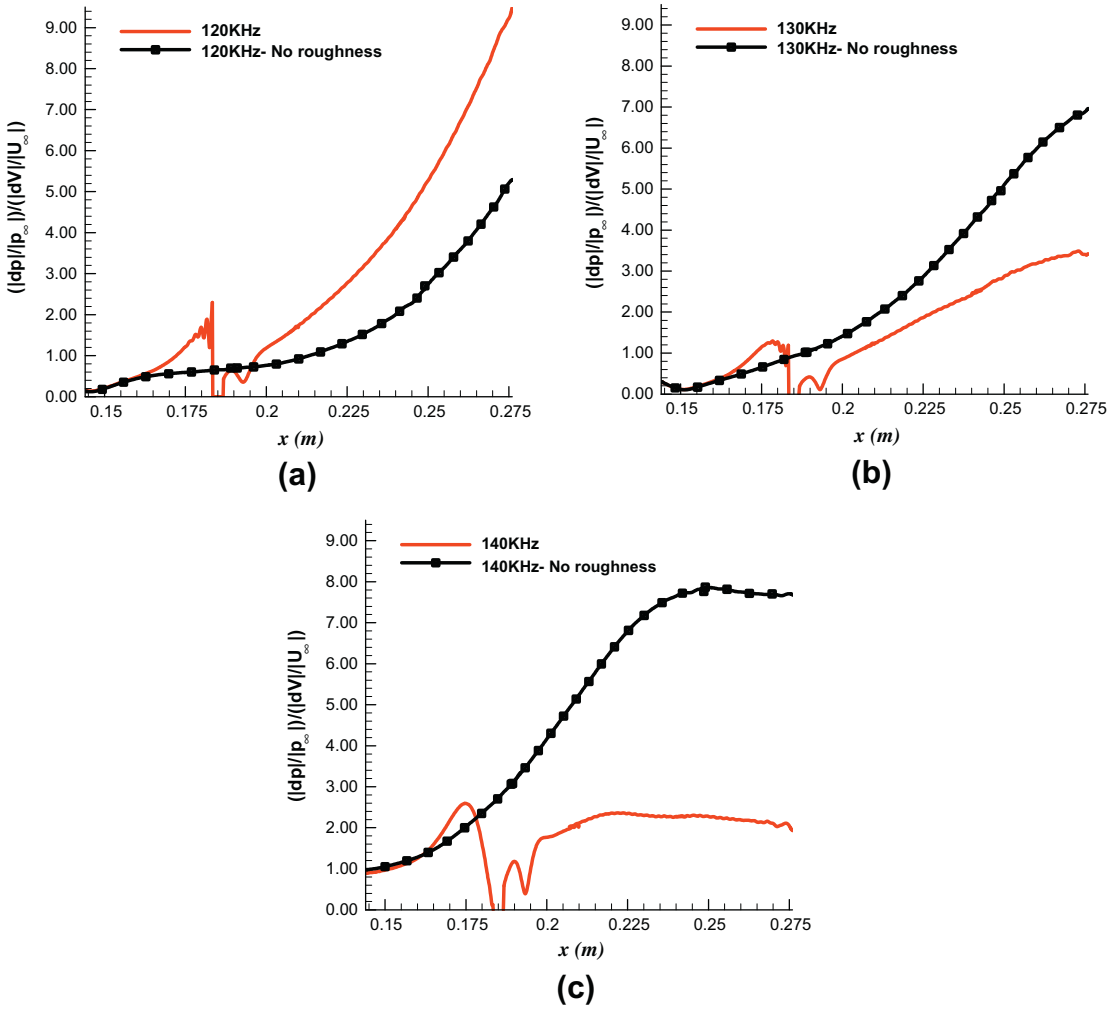

Fig. 22. Spatial evolution of wall pressure perturbation at three different frequencies (a) 120 kHz, (b) 130 kHz and (c) 140 kHz.

compared with the no roughness case. However, frequencies around 133.26 kHz are all highly damped. The frequency range of the damping effect is from approximately 120 kHz to 170 kHz. It can also be seen that the strongest damping occurs very close to the synchronization frequency. As the perturbation travels downstream, the high frequency perturbations (around 140–170 kHz) that have been damped in the previous location drop even further. Meanwhile, perturbations at frequencies around 133.26 kHz start

Please cite this article in press as: Fong KD et al. Numerical simulation of roughness effect on the stability of a hypersonic boundary layer. Comput Fluids (2014), http://dx.doi.org/10.1016/j.compfluid.2014.01.009

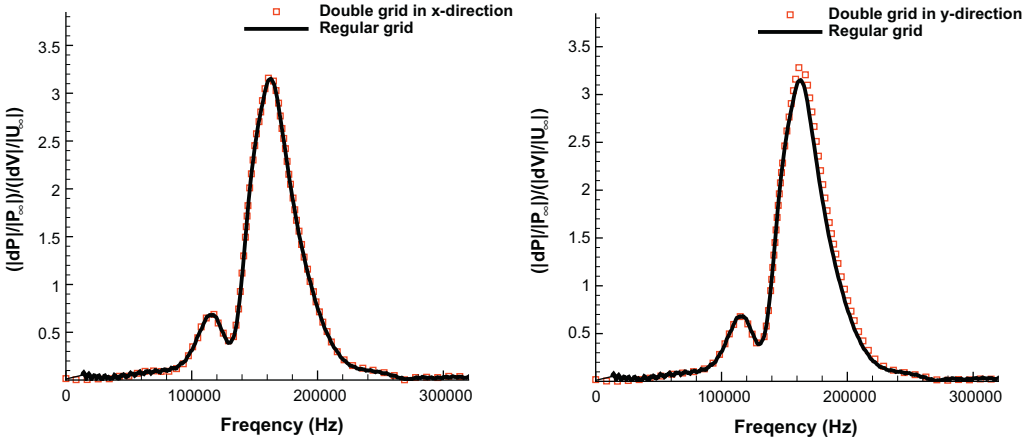

Fig. 23. Non-dimensional frequency spectra of wall pressure perturbation at $x = 0.186$ m for double grid in x-direction and double grid in y-direction.

to grow at a slow rate. For the amplified perturbations at frequencies around 120 kHz, the growth is very strong, and the perturbation amplitude is always greater than the no roughness case. The FFT results from upstream and downstream of the roughness show that a two dimensional roughness is capable of amplifying perturbations at frequencies lower than the synchronization frequency, while damping frequencies close to and higher than the synchronization frequency.

Fig. 22 shows the normalized amplitude of wall pressure perturbations at three different frequencies in the stream wise direction. In particular, we are interested in the frequencies higher than, close to, and lower than the synchronization frequency of 133.26 kHz. Therefore 120 kHz, 130 kHz and 140 kHz are chosen. For comparison, their evolution in the case without roughness is also included. It can be clearly seen that the perturbation at 120 kHz is highly amplified due to roughness because it is lower than the synchronization frequency. Its amplitude is almost twice that of the case without roughness at $x = 0.275$ m. However, the perturbation at 130 kHz, which is close to the synchronization frequency, is damped compared with the no roughness case. Without roughness, the perturbation at this frequency grows exponentially and it reaches a normalized amplitude of almost 4 at $x = 0.275$ m. With roughness, this perturbation is amplified far upstream of roughness. As it gets closer to the roughness, it starts to be damped significantly. Its normalized amplitude only reaches about 2.5 at the end of the figure. For the perturbation at 140 kHz, the damping effect is even more pronounced than the previous case because it is higher than the synchronization frequency. As shown in Fig. 22(c), its normalized amplitude grows to around 8 without roughness. On the other hand, with the existence of roughness, the amplitude level stays near 2 at $x = 0.275$ m.

4.7. Grid independence study for unsteady simulations

Similar to the steady flow grid study, it is important to validate grid independence for unsteady simulations. The x-direction double grid steady flow and the y-direction double grid steady flow in Section 4.3 are used for unsteady grid independence study. The same pulse model in Section 4.6 is imposed onto the two mean flows respectively to disturb the flows. The same FFT technique is utilized to study the spatial growth of pressure perturbation. Fig. 23 shows the frequency spectra for double grid in the x-direction and the y-direction compared with the regular grid. The frequency spectra are taken at $x = 0.186$ m. As previously mentioned in Section 4.3, this location is close to the roughness element and is sensitive to grid changes. As can be seen from Fig. 23, the frequency spectra for the two double grid sets agree very well with the frequency spectrum obtained from the regular grid. It is concluded that the unsteady simulations are grid independent.

4.8. The effect of two roughness elements

The effect of multiple roughness elements is considered in this section. The first roughness is at the same location as case 2, $x_r = 0.185$ m. The first roughness height is fixed at 50% of the local boundary layer thickness. The second roughness is placed in the downstream region of the first roughness at $x_r = 0.231$ m, while its height is kept the same as the first roughness. The location of the first roughness corresponds to the synchronization point frequency for 133.26 kHz, while the location of the second roughness corresponds to the synchronization point frequency for 119.26 kHz.

The same pulse model is imposed onto the mean flow. Fig. 24 shows the pressure contour of the two roughness mean flow. It is seen that the second roughness generates the same Mach waves as the one roughness case. In the unsteady simulation, the perturbation has a frequency range of 1 MHz as in Fig. 15. The pressure perturbation contour is shown in Fig. 25. Similar to the one

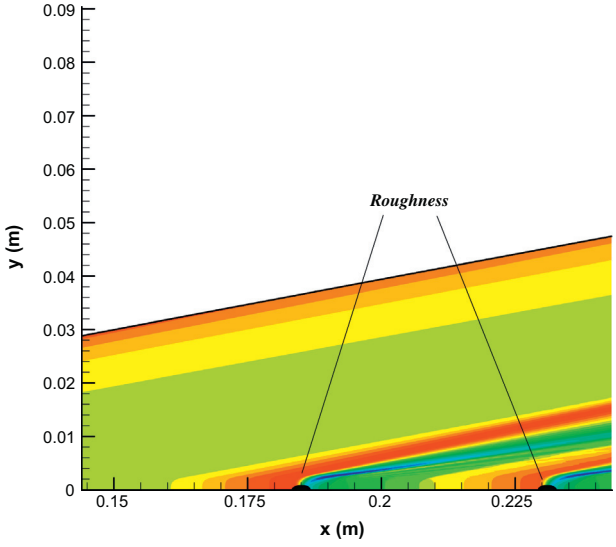

Fig. 24. Pressure contour of the two roughness meanflow.

Please cite this article in press as: Fong KD et al. Numerical simulation of roughness effect on the stability of a hypersonic boundary layer. Comput Fluids (2014), http://dx.doi.org/10.1016/j.compfluid.2014.01.009

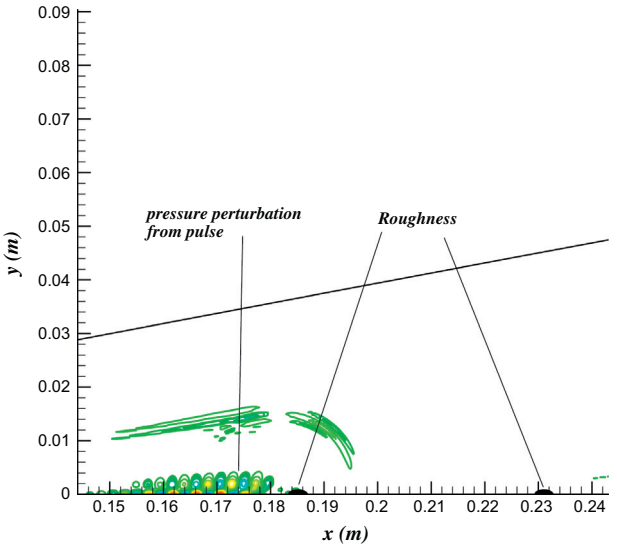

Fig. 25. Pressure perturbation contour for the two roughness case.

roughness case, it is of interest to study how the perturbation interacts with the two roughness elements. Fig. 26 shows the spatial development of perturbations at different frequencies. Similar to Fig. 22, the frequencies chosen are 120 kHz, 130 kHz and 140 kHz. Since the location of the second roughness corresponds to the synchronization point frequency of 119.26 kHz, it is expected that the perturbations at these three frequencies will be damped after the second roughness. Fig. 26 confirms the expectation. It is shown that the first roughness amplifies the 120 kHz perturbation since it is upstream of its synchronization point. However, when the perturbation travels downstream and approaches the second roughness, it starts to be damped since the second roughness is located very close to its synchronization point. Downstream of the second roughness, the perturbation at 120 kHz is weaker than the case without roughness. For 130 kHz and 140 kHz perturbations, both roughness elements are located downstream of their synchronization points. Therefore, the two roughness elements both have a damping effect on these two frequencies as expected. Fig. 26(b) and (c) show this trend. It is also seen that the damping effect is more pronounced in the two roughness case than in the one roughness case.

5. Conclusion

The effect of two dimensional roughness on modal growth of a Mode S perturbation and a perturbation with a wide frequency spectrum on a hypersonic flat plate at Mach 5.92 has been investigated. The numerical method is the new high order cut-cell method. One and two roughness elements cases and the effect of

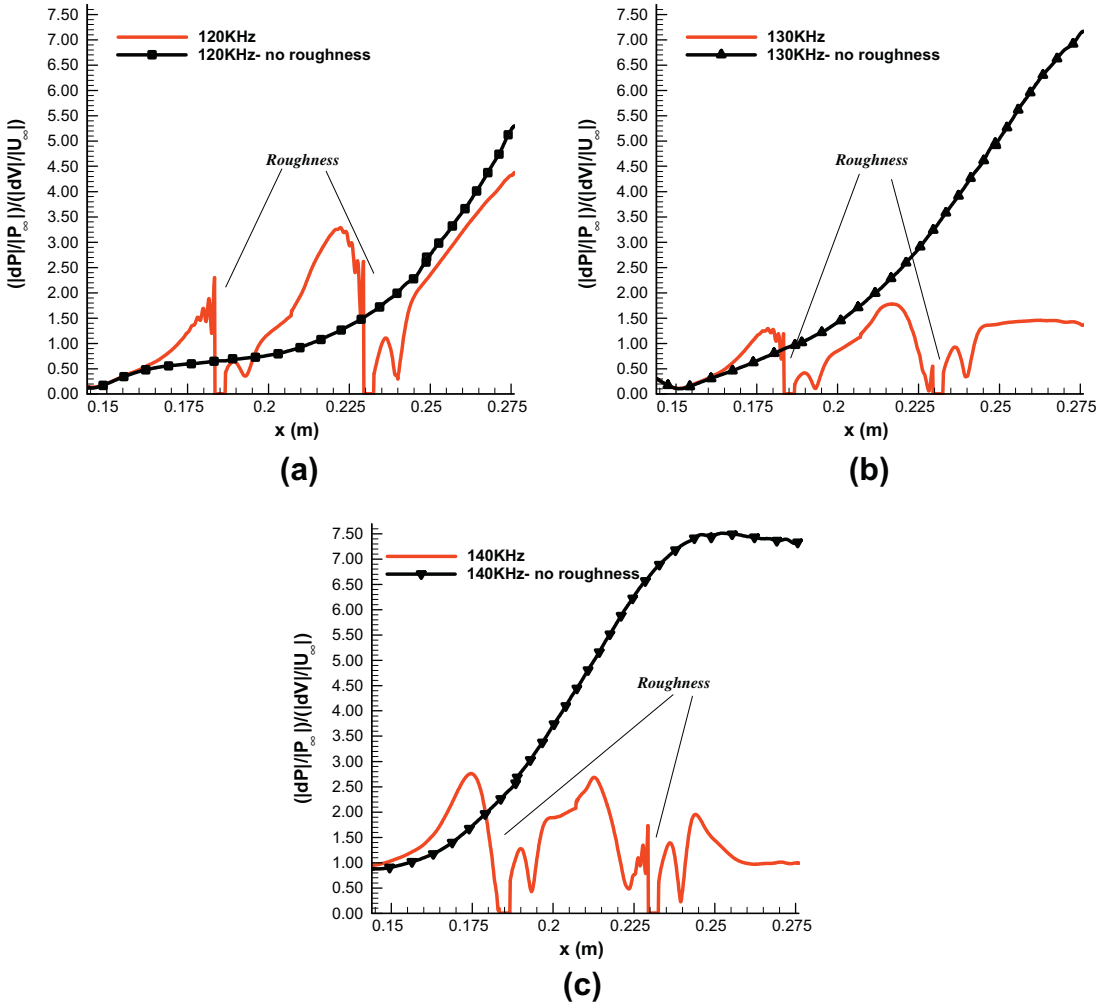

Fig. 26. Spatial evolution of wall pressure perturbation for the two roughness case at three different frequencies (a) 120 kHz, (b) 130 kHz and (c) 140 kHz.

Please cite this article in press as: Fong KD et al. Numerical simulation of roughness effect on the stability of a hypersonic boundary layer. Comput Fluids (2014), http://dx.doi.org/10.1016/j.compfluid.2014.01.009

roughness height have also been studied. The results confirmed previous findings in Duan et al. [17] and Fong et al. [19] that a roughness element is capable of amplifying perturbations at a certain frequency if the roughness element is placed upstream of the synchronization point. On the other hand, if a roughness element is placed downstream of the synchronization point, the perturbations which have higher frequencies will be damped. It has also been found that if the roughness height is less than the local boundary layer thickness, large roughness element results stronger amplification or stronger damping depending on the roughness location. The numerical results of both steady and unsteady simulations have been validated in grid independence studies. The numerical results provide an explanation of roughness delay transition as shown in some experiments [15,16]. Using this information can provide a new way to control boundary layer transition by using two dimensional surface roughness. In the future, we will extend our study from two dimensions to three and study 3D roughness effect.

Acknowledgments

This work was sponsored by the Air Force Office of Scientific Research, USAF, under AFOSR Grant FA9550-07-1-0414, monitored by Dr. John Schmisseur, and by the National Science Foundation, Award ID 0933556. This work was also sponsored by the AFOSR/NASA National Center for Hypersonic Research in Laminar–Turbulent Transition. The views and conclusions contained herein are those of the author and should not be interpreted as necessarily representing the official policies or endorsements either expressed or implied, of the Air Force Office of Scientific Research or the U.S. Government.

References

[1] Schneider S. Summary of hypersonic boundary-layer transition experiments on blunt bodies with roughness. J Spacecraft Rockets 2008;45:1090–112.
[2] Board D. Final report of the second defense science board task forces on the national aero-space plane. Tech. Rep. NASP; 1992.
[3] Berry S, Horvath T. Discrete roughness transition for hypersonic flight vehicles. AIAA paper 2007-0307; 2007.
[4] Saric W, Reed H, Kerschen E. Boundary-layer receptivity to freestream disturbances. Annu Rev Fluid Mech 2002;34:291–319.
[5] Mack L. Boundary-layer linear stability theory. Advisory Group for Aerospace Research and Development; 1984. p. 709.
[6] Maslov A, Shiplyuk A, Sidorenko A, Arnal D. Leading-edge receptivity of a hypersonic boundary on a flat plate. J Fluid Mech 2001;426:73–94.
[7] Maslov A, Mironov S, Shiplyuuk A, Sidorenko A, Buntin D, Aniskin V. Hypersonic flow stability experiments. AIAA paper 2002-0153; 2002.
[8] Demetriades A. Hypersonic viscous flow over a slander cone. Part III: Laminar instability and transition. AIAA paper 74-535; 1974.
[9] Demetriades A. Laminar boundary layer stability measurements at mach 7 including wall temperature effects. AFOSR-TR 77-1311; 1977.
[10] Malik M, Lin R, Sengupta R. Computation of hypersonic boundary-layer response to external disturbances. AIAA paper 1999-0411; 1999.
[11] MA Y, Zhong X. Receptivity to freestream disturbances of mach 8 flow over a sharp wedge. AIAA pa 2003-0788; 2003.
[12] Wang X, Zhong X, Ma Y. Response of a hypersonic boundary layer to wall blowing – suction. AIAA 49-7:1336–53; 2011.
[13] Balakumar P. Transition in a supersonic boundary-layer due to roughness and acoustic disturbances. vol. 3589. AIAA; 2003.
[14] Marxen O, Iaccarino G. Numerical simulation of the effect of a roughness element on high speed boundary layer instability. In: 38th Fluid dynamics conference and exhibit; 2008.
[15] Holloway P, Sterett J. Effect of controlled surface roughness on boundary-layer transition and heat transfer at mach number of 4.8 and 6.0. Tech. rep. D-2054. NASA Technical Note; 1964.
[16] Fujii K. An experiment of two dimensional roughness effect on hyper-sonic boundary-layer transition 2005-891; 2005.
[17] Duan L, Wang X, Zhong X. A high-order cut-cell method for numerical simulation of hypersonic-boundary transition with arbitrary surface roughness. AIAA paper 2009-1337; 2009.
[18] Duan L, Wang X, Zhong X. Stability of a mach 5.92 flat-plate boundary layer with the effect of 2-d finite height roughness. AIAA J 2013;51:266–70.
[19] Fong K, Wang X, Zhong X. Finite roughness effect on modal growth of a hypersonic boundary layer. AIAA paper 2012-1086; 2012.
[20] Duan L, Wang X, Zhong X. A high order cut cell method for numerical simulation of hypersonic boundary-layer instability with surface roughness. J Comput Phys 2010;229:7207–37.
[21] Whitehead A. Flow field and drag characteristics of several boundary-layer tripping elements in hypersonic flow. Tech. rep. Techinical paper, NASA; 1969.
[22] Klebanoff P. Mechanism by which a two-dimensional roughness element induces boundary-layer transition. Phys Fluids 1972;15–7:1173–88.
[23] Malik M, Spall R, Chang C. Effect of nose bluntness on boundary layer stability and transition. AIAA paper 90-0112; 1990.
[24] Fedorov A, Khokhlov AP. Prehistory of instability in a hypersonic boundary layer. Theor Comput Fluid Dynam 2001;14:359–75.
[25] Wang X, Zhong X. Effect of wall perturbations on the receptivity of a hypersonic boundary layer. Phys Fluids 2009. 21-044101.
[26] Marxen O, Laccarino G, Shaqfeh E. Disturbance evolution in a mach 4.8 boundary layer with two-dimensional roughness-induced separation and shock. J Fluid Mech 2010;648:435–69.